2018-01-01

Evaluation Of Large Area Additively Manufactured Fiber Reinforced Acrylonitrile Butadiene Styrene (abs)

Kevin Schnittker
University of Texas at El Paso, kschnittker4@gmail.com

EVALUATION OF LARGE AREA ADDITIVELY MANUFACTURED FIBER REINFORCED ACRYLONITRILE BUTADIENE STYRENE (ABS)

KEVIN SCHNITTKER

Master's Program in Metallurgical and Materials Engineering

APPROVED:

David A. Roberson, Ph.D., Chair

Stephen W. Stafford, Ph.D.

Calvin Stewart, Ph.D.

Charles Ambler, Ph.D.
Dean of the Graduate School

Dedication

To God and My Loving Family,

Who have supported me through this endeavor.

EVALUATION OF LARGE AREA ADDITIVELY MANUFACTURED FIBER REINFORCED ACRYLONITRILE BUTADIENE STYRENE (ABS)

by

KEVIN SCHNITTKER, BSMME

THESIS

Presented to the Faculty of the Graduate School of

The University of Texas at El Paso

in Partial Fulfillment

of the Requirements

for the Degree of

MASTER OF SCIENCE

Department of Metallurgical, Materials and Biomedical Engineering

THE UNIVERSITY OF TEXAS AT EL PASO

December 2018

Acknowledgements

I would like to thank Dr. Roberson for his mentorship and friendship throughout my time at The University of Texas at El Paso. Dr. Roberson was the first professor to offer me an opportunity to do research as an undergraduate. Through those experiences working within his Polymer Extrusion Lab (PEL) propelled me to stay at UTEP and continue my education. My time as a graduate student and working under Dr. Roberson helped me to learn and admire the type of person David is, someone who will go out of their way to help a student. That passion to help others succeed motivated me to continue developing my academic career and work towards a Ph.D. in Materials Science. My sincere gratitude to Dr. Stafford for all his invaluable teachings and providing me with a long-lasting impression on the importance of material characterization. Thank you, Dr. Stewart for allowing me to have access to your DIC equipment for the duration of this study. The data collected from the DIC constitutes a large portion of this thesis.

I would like to acknowledge Katherine Heidi Fehr for all her support and technical expertise. Heidi, thank you for always standing by my side and encouraging me to reach my highest potential. To Dr. Schnittker, thank you for taking the time to help review my thesis and provide valuable input, you have always been a loving sister to me.

To the current and past members of Dr. Roberson's polymer extrusion lab: Gilberto Siqueiros, Adriana Ramirez, Francisco Andrade, Israel Carrete, Truman Word, Evelyn Vazquez, and Diego Bermudez thank you all for your encouragement and friendship these past few years. You are all some of the finest researchers UTEP has to offer. To Edel Arrieta for his expertise with DIC technology, none of the work presented here could have been possible without your guidance. Finally, thank you Xavier Jimenez for all your help printing specimens on the BAAM – 100 system.

Abstract

To enable the advancement of large-scale additive manufacturing processes, it is necessary to establish and standardize methodologies to characterize the mechanical properties of printed test coupons. Due to the large size of the print beads, conventional test standards are inadequate. The focus of this study was to determine the feasibility of using Digital image correlation (DIC) technology as a key enabler for robust data collection of strain measurements of large 3D printed parts. To incorporate the DIC measurements, a novel method was developed to prepare large 20 wt.% glass filled ABS test coupons for adequate contrast. Through this technique, Poisson's ratio and elastic modulus were measured and stress strain curves were generated. The data produced by DIC collaborated well with failure analysis performed on spent test coupons. Additionally, fracture surface analysis of the specimens revealed poor adhesion among the ABS matrix and glass fibers. This matrix/fiber debonding demonstrated the need for improved printing parameters to maximize tensile strength. Finally, critical length analysis of the fibers revealed them to be dimensionally inadequate, prompting a need for extrusion parameters to be optimized. The bead neck growth study conducted on 20 wt.% carbon fiber filled ABS provided insight on the screw speed limitation at which this material could be processed. The work presented here establishes the framework for future characterization of BAAM fabricated components.

Table of Contents

Acknowledgements v

Abstract vi

List of Tables ix

List of Figures x

Chapter 1: Statement of Purpose 1

Chapter 2: Background 3

2.1 Extrusion Background 3

2.2 Single Screw Extrusion 3

2.3 Twin Screw Extrusion 5

2.4 Fused Deposition Modeling 7

2.5 Big Area Additive Manufacturing 10

2.6 Material Extrusion Build Parameters 11

Chapter 3: Mechanical Characterization of Large Area Additive Manufactured Components 16

3.1 Case Studies 17

3.2 Digital Image Correlation 17

Chapter 4: Experimental Procedures 19

4.1 Material Selection 19

4.2 BAAM Extrusion Parameters 22

4.3 Rheology 23

4.4 Critical Fiber Length 24

4.5 Single Bead Characterization 24

4.6 Tensile Specimens 25
4.7 Tensile Test 27
4.8 Fractography 29
4.9 Neck Growth Variation between ABS-20GF Tensile Samples 29
4.10 Neck Growth and Screw Speed Relationship 30
Chapter 5: Results and Discussion 32
5.1 Rheological Results 32
5.2 ABS-20GF Single Bead Characterization 32
5.3 Tensile Results 33
5.4 Fractography 39
5.5 Critical Fiber Length 42
5.6 Neck Growth Variation between ABS-20GF Tensile Samples 43
5.7 Neck Growth and Screw Speed Relationship for ABS-20CF Samples 44
Chapter 6: Conclusion 48
6.1 Future Work 49
Chapter 7: References 50
Vita 54

List of Tables

Table 4.1: Measured resistance of the ABS-20%CF block at different currents, see Figure 4.1 for measurement reference 22
Table 4.2: BAAM parameters for glass fiber and carbon fiber ABS..... 23
Table 5.1: Melt Flow Index Results 32
Table 5.2: Mechanical properties of the ABS-20GF coupons..... 34
Table 5.3: Measured fiber length of the ABS-20GF composite blend, before and after extrusion..... 43

List of Figures

Figure 2.1: Single screw extrusion methodology [16] 5
Figure 2.2: Diagram of the various screw configurations of twin-screw extrusion [16] 6
Figure 2.3: Extrusion screw configurations within film blowing and compounding/pelletizing [16] 7
Figure 2.4: Break down of an FDM system [25] 9
Figure 2.5: Different raster orientations used in 3D printing: 0° (a), 45° (b), 90° (c), 45° & -45° (d) [25] 13
Figure 2.6: Illustration of the different air gaps formed in AM material extrusion [21] 14
Figure 2.7: Model of the neck growth among two deposited beads [36] 15
Figure 4.1: Image of the wire embedded block (a) reference image where resistance measurements we taken (b) 22
Figure 4.2: Tinius Olsen MP1200 Melt Flow Indexer 24
Figure 4.3: Mounted and polished single bead showing the horizontal cross section (a) the vertical cross section 25
Figure 4.4: Image of the printed hexagon showing the location of each specimen, green arrows indicate build direction, and red circle specifies seam edge 26
Figure 4.5: Large tensile specimen dimensions (mm), thickness of 19 mm (a) Image of harvested tensile specimen (b) 26
Figure 4.6: Specimen with optical instrumentation setup (a) grips, (b) cameras, and (c) specimen. 27
Figure 4.7: (a) Speckle pattern applied on the tensile test specimen. (b) Uncertainty in the correlation of subsets in images 28
Figure 4.8: Illustration of where the neck size measurement we taken 30
Figure 4.9: Dimensions (mm) of the trapezoidal test structure, thickness was 4 layer or 15.24 mm 31
Figure 4.10: Image of the cross sectioned ABS-20CF samples used to measure neck formations 31
Figure 5.1: SEM images of the ABS-20GF single bead, vertical cross section (a) horizontal cross section (b) 33

Figure 5.2: ABS-20GF Stress-Strain Curves 36
Figure 5.3: Virtual extensometers placed on the fracture site 37
Figure 5.4: DIC strain fields of the ABS-20GF specimen at the midpoint of the tensile test 38
Figure 5.5: DIC strain fields on ABS-20GF specimens at an instant before rupture..... 38
Figure 5.6: Fracture surface images of the tensile specimens (a,b) crack initiation site for tensile sample 4, (c,d) tensile sample 5 40
Figure 5.7: Images of fracture surface of sample 5, (a) photograph of a print gap, (b-d) SEM images of the fracture surface. 41
Figure 5.8: SEM image of the bond between two layers. 42
Figure 5.9: Variation of neck sizes between specimen 2 and 5 for an ABS-20GF blend 44
Figure 5.10: SEM images of the ABS-20CF vertical cross-sectional view extruded at 50 (a), 150 (b). 250 (c), 350 (d), and 400 rpms (e)..... 46
Figure 5.11: Neck size measurements of ABS-20CF specimens extruded at 50 and 150 rpms 47

Chapter 1: Statement of Purpose

The main method of additively manufactured thermoplastic polymers is material extrusion [1]. In simple terms, material extrusion is the selective deposition of material through a nozzle or orifice [1]. One of the most common and developed processes within the material extrusion category is fused deposition modeling (FDM). The Industrial Grade FDM units offered by Stratasys since the early 1990s have a tool head that move in the XY plane and a moving build platform that descends in the Z-axis after completion of a given layer [2], [3]. The feedstock for these types of printers are a polymer monofilament that can be heated and melted.

As the original FDM patent expired in 2009 [4], many new iterations of the technology have been realized, primarily in the low-cost, desktop category [5]. These open-source printers are generally referred to as fused filament fabrication (FFF) machines [2], [3]. Key differences between FDM systems and low-cost variants involve movement of the print head and the build platform as well as nuances related to creating a temperature-controlled environment within an isolated build chamber, a feature still exclusive for FDM. Another implementation of FDM technology has been the incorporation of multi-material printing to produce multifunctional products [6]. The development of multi-process additive manufacturing [7], [8], which interrupts an FDM build to allow for the selective placement of a conductive metal wire or electrical component, has evolved the state of FDM structures. Printed parts can now be embedded with sensors and actuators, further expanding their practicality within the aerospace, defense, and biomedical industries [7], [9].

Despite the evolution of the FDM process within diverse industries, the system is innately limited by its build volume and the deposition rate of the polymer melt. Due to the FDM and FFF reliance on a monofilament as a feedstock, the rate at which material can be deposited will always be restricted. These constraints led to the development of Big

Area Additive Manufacturing (BAAM) through the collaboration between Oak Ridge National Labs (ORNL) and Cincinnati Incorporated [10]. This manufacturing processes involves the use of a pellet-fed single screw extruder that propels the system to sustain deposition rates that are 200 times faster than conventional AM printers [11]. The onset of this novel 3D printer has the potential to dramatically change the practicality of material extrusion additive manufacturing. Within multi-process AM, large-scale components can be printed at reasonable rates and have electrical components embedded within the structure. A general example would be an expansion of the energy efficient home manufactured through a BAAM process [12]. Using a multi-process AM technique, energy efficiency would further improve due to the incorporation of electrical components within the build. However, before these multifunctional products can be conceptualized, a clear understanding of the mechanical properties of BAAM fabricated components must be identified.

The aim of this study is to build upon the mechanical testing strategies currently used to characterize BAAM components, to provide a foundation for material design, and to push this technology into multi-process AM applications. The introduction of digital image correlation (DIC) equipment to offset the limitations of traditional equipment and the expansion of the relationship between extruder screw speed and interlayer bonding is the focus in this work. The incorporation of DIC with large-scale polymer fiber reinforced test coupons/specimens, manufactured by a BAAM process, enabled additional mechanical properties of the printed specimens to be determined. Fiber reinforced test coupons were analyzed on a scanning electron microscope (SEM) to characterize the failure mechanisms present in the fiber reinforced test coupons. Additionally; the microstructure, fiber orientation, and bead neck growth were observed to determine print quality.

Chapter 2: Background

2.1 Extrusion Background

The primary thermoplastic manufacturing techniques are extrusion and injection molding. Both processes involve a resin, in the form of pellets, being fed through a heated barrel by a screw or set of screws. Of these two methods, extrusion dominates the world market by consuming approximately 36 wt.% of all processed plastics [13]. The first rendition of an extruder came in 1797 when J. Bramah built a ram extruder to produce seamless lead pipes [14]. The process involved maintaining lead (Pb), or another soft metals, in a molten state that was then forced into a long projecting tube (the die) by a positive displacement pump [15]. A positive displacement pump is categorized as a noncontinuous process as the system is reliant on moving a fixed amount of material that is displaced.

Due to the noncontinuous nature of a ram extruder, scientists sought for a mean that was continuous to be used in the wire/cable coating industry [16]. Thus, M. Gray patented the first single screw extruder used for wire coating in 1879 [16]. Unlike ram extruders, which involve a positive displacement pump to produce a pressure rise, screw extruders use a viscosity pump to produce a pressure gradient from the difference of the deviatoric stress tensor (fluid deformation) [17]. The first screw extruder designed specifically for a thermoplastic came in 1935 by P. Troester [18].

2.2 Single Screw Extrusion

Currently, screw extruders can be categorized as either a single screw extruder or a twin-screw extruder. A single screw extruder is widely used within the polymer industry due to its versatility in carrying out extrusion processes, such as blow and film molding, while being a part of the standard injection molding unit [17]. A single screw extruder can be spilt into three zones: compaction, melting, and pumping. An illustration of a single

screw extruder is depicted in Figure 1. In the compaction, or solid conveying zone, resin pellets loaded in the hopper are deposited into the screw channel. The pellets are fused together due to a high coefficient of friction between the barrel surface and the screw surface [16]. A high coefficient of friction is maintained by cooling the barrel in the compaction zone, depicted as the “cooling jacket” in Figure 2.1. As the compacted pellets are transported through the screw channel, they enter the transition zone (melting phase) where the material begins to melt. Recalling that the barrel is heated, this causes the surface of the compacted resin to melt, forming a melt film [16]. As the resin is pumped through the screw, the molten polymer is wiped from the melt film forming a melt pool ahead of the compacted resin [16], [17], [19]. The plastic melt continues to move through the screw channel in a spiral manner and enter the metering zone (pumping). In this phase, the plastic melt shears and subsequently mixes in this region [18]. The metering zone also is also extremely important in generating pressures sufficient for pumping through an orifice or die [17]. When the molten resin exits the barrel, the extrusion die is responsible for forming the final shape/profile of the thermoplastic. In single screw extrusion, the relationship between the barrel length (L) and the screw diameter (D), expressed as the L/D ratio, is a measure of an extruder’s throughput capacity. An extruder with a large L/D has a higher capacity of melting and mixing (a higher throughput) than an extruder with a smaller L/D [19], [20]. However, a higher L/D extruder comes at a much higher initial investment cost than an extruder with a small L/D.

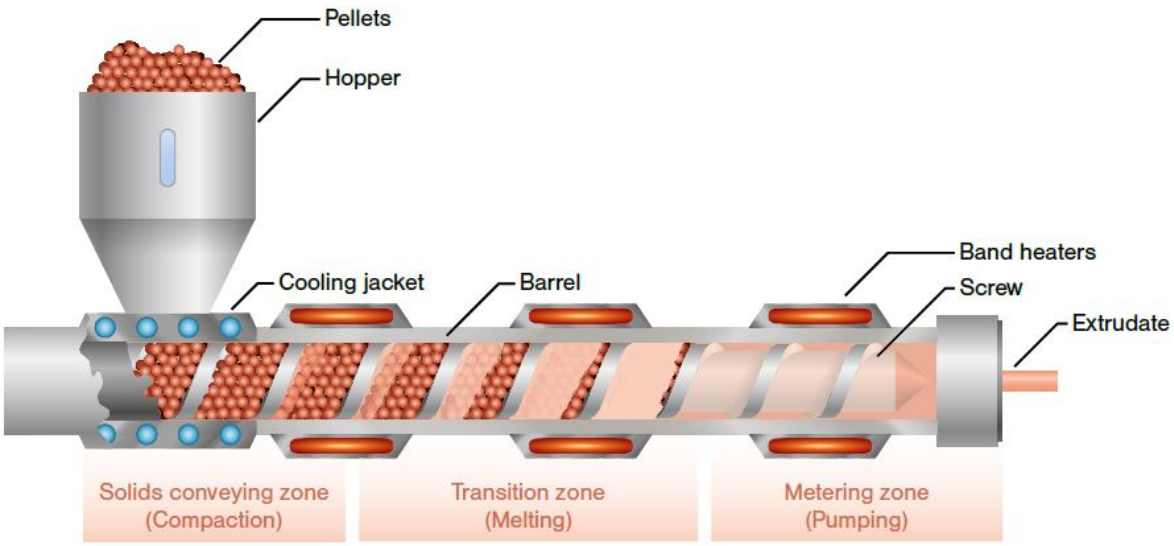

Figure 2.1: Single screw extrusion methodology [17]

2.3 TWIN SCREW EXTRUSION

A twin screw extruder operates much like a single screw extruder; however, offers a greater capability of mixing due to the incorporation of two screws within a twin barrel. Figure 2.2 depicts the different screw configurations of a twin screw extruder. The two screws can either rotate in the same direction (corotating) or rotate in opposite directions (counterrotating). In addition, the screws can either have a centerline gap less than the screw diameter (called intermeshing) or a centerline gap equal to the screw diameter (called non-intermeshing) [21].

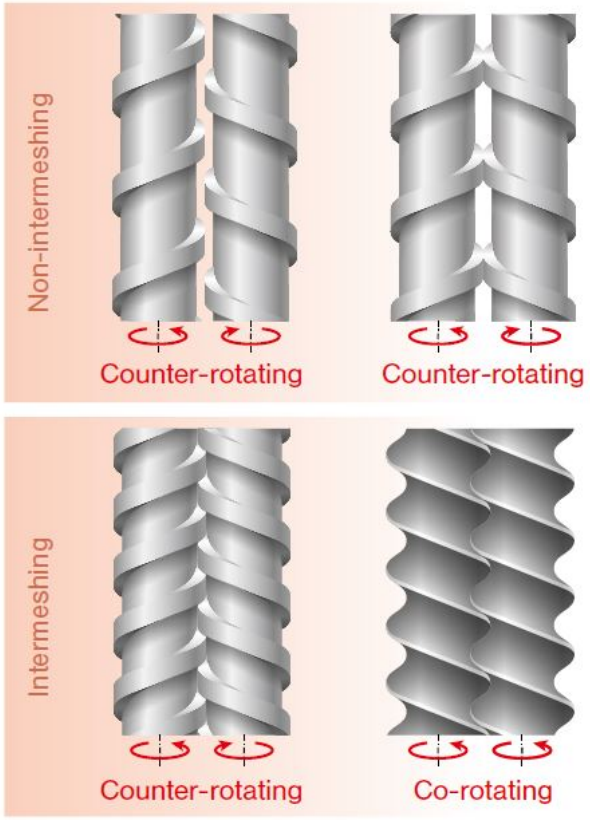

Figure 2.2: Diagram of the various screw configurations of twin-screw extrusion [17]

Thermoplastic resin fed into a twin-screw extruder will progress through the same three zones (compaction, melting, and pumping) mentioned for single screw extruders (See Section 2.2). The key difference is the greater degree of achievable shear on the plastic melt within the pumping/metering zone. As a result, more mixing capability among the plastic melt. Figure 2.3 shows a diagram of the different extrusion processes (film blowing, monofilament fabrication, and composite compounding) and their respective screw(s) configurations.

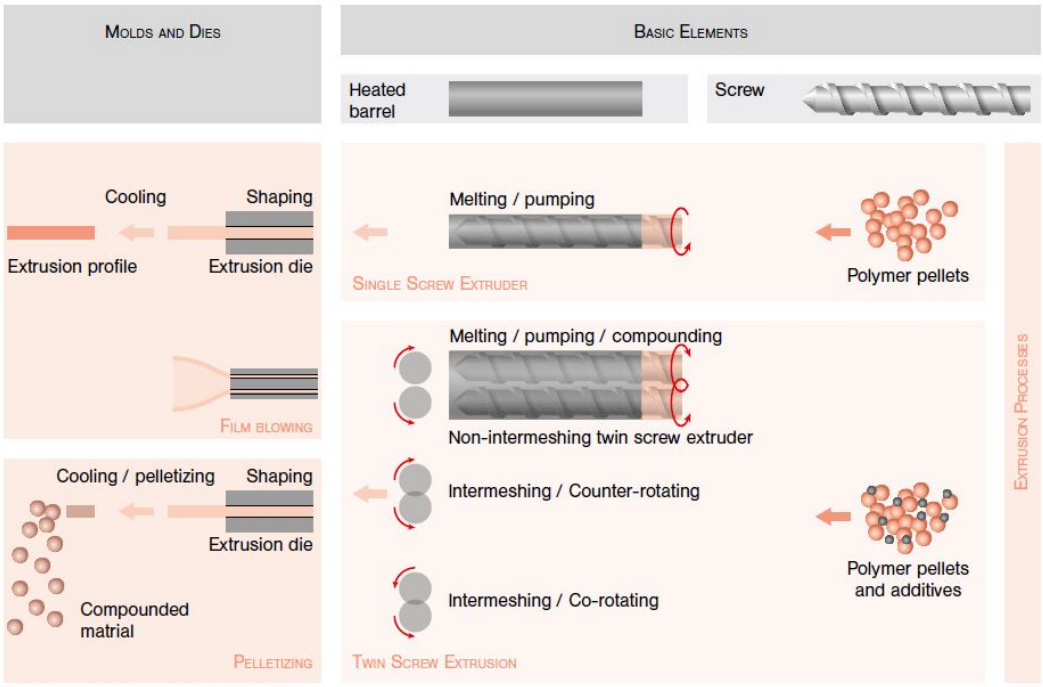

Figure 2.3: Extrusion screw configurations within film blowing and compounding/pelletizing [17]

2.4 Fused Deposition Modeling

One of the most common and developed routes in additive manufacturing (AM) is the thermoplastic material extrusion process. The earliest rendition of the material extrusion process came in the early 1989 when S. Crump, the Founder of Stratasys, Inc., patented the fused deposition modeling (FDM) method [3], [22], [23]. AM technology heats a thermoplastic, or thermoplastic matrix composite, material into a liquid state that is selectively deposited through a nozzle/orifice [22], [24] as shown in Figure 2.4. The liquefier head follows a toolpath in the X and Y axis that is predetermined based off slicing a computer-aided design (CAD) model in a layer by layer manner. In the fabrication of a three-dimensional object, the build stage moves in the Z direction when the liquefier head completes a layer. The primary feedstock for these systems is a thermoplastic monofilament generally 1.75 mm in diameter, though there are platforms that utilize a 2.85 mm diameter filament. Plastic monofilaments, depending on the manufacturer or

source, are processed via single/twin screw extrusion. The entire workflow of the FDM process can be generalized as the following [3], [25]:

- Modeling of the 3D object, using a CAD software
- Conversion of the CAD design into a standard tessellation language (STL) or etc. which is manipulated, sliced, and then transferred to the printer.
- Machine Setup
- Build/Printing
    - Material feedstock: Monofilament
    - Liquefier head moves in the X and Y axis, stage moves down in the Z axis
- Part Removal
- Post Processing

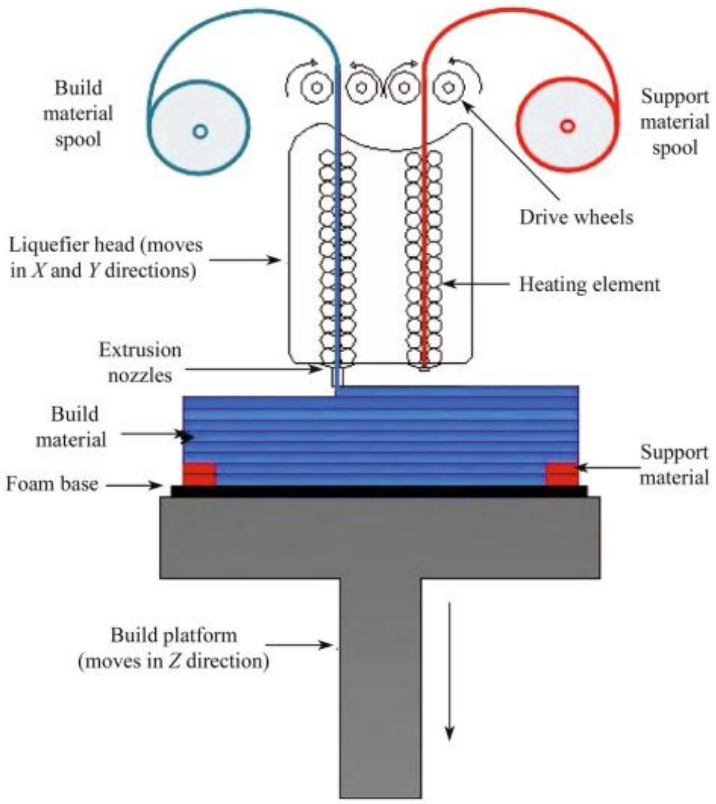

Figure 2.4: Break down of an FDM system [26]

The advent of the FDM material extrusion process allowed for rapid and low-cost prototyping within the aerospace, dental, architecture, and medical industries [27], [28]. Currently, FDM systems are commonly used within the education sector to promote enhanced hands on experiences for students [29]. However, the FDM process suffers from many drawbacks, limiting its use within an industry. The primary challenges are the build speed, accuracy and density of the printed component [30]. To achieve a more dimensionally accurate and stronger component, smaller nozzle sizes and layer heights are needed at the expense of an increase build time. Generally, FDM is employed within an industry for the sole purpose of prototyping, due to the low costs associated, then when a design is finalized the FDM process is replace with traditional polymer processing techniques. There is a demand to use FDM as means to fabricate a final component due

to its freedom of design. The process is not limited to traditional design criteria due to the layer by layer manufacturing.

2.5 Big Area Additive Manufacturing

As the original FDM patents expired, many new implementations of the technology have been realized; including low-cost desktop systems [4] and large area additive manufacturing. Through the collaboration of Oak Ridge National Laboratory and Cincinnati Incorporated, the Big Area Additive Manufacturing (BAAM) 3D printer was developed [10]. A BAAM printer is essentially a scaled-up version of the traditional thermoplastic FDM printer, in that both selectively deposit plastic material through a nozzle to form a 3D object in a layer by layer manner. The main difference is that, as its name implies, the BAAM system has a build volume substantially greater then common FDM printers. The BAAM systems boast build volumes of up to 6.1 x 2.3 x 1.8 m and allow the fabrication of very large structures at extremely high material deposition rates, 36.3 kg/hour [31], [32]. Aside from a BAAM printer being larger than an FDM system, they're equipped with a pellet-fed single screw extruder rather than a nozzle that liquefies a monofilament. Thus, the control of plastic flow and rheology is more comprehensive within a BAAM printer as compared to FDM. Finally, unlike FDM, a BAAM printer is equipped with a Z-tamping attachment to compact the extruded plastic material around the nozzle as it is being deposited [10]. The compaction of the deposited bead improves consolidation between layers and reduces the creation of voids between successive beads [11]. A tamper typically vibrates along the layer surface at frequency of 20 Hz. The work flow for a BAAM printer is generalized as the following [11], [25], [32]:

- Modeling of the 3D Object, using a CAD software
- Conversion of the CAD design into an STL, AMF, 3MF, file or etc. which is manipulated, sliced, and then transferred to the printer.
- Machine Setup

- Build/Printing
    - Material feedstock: Resin pellets
    - Liquefier head move in the X and Y axis, stage moves down in the Z axis
    - Equipped with a Z-tamping attachment
- Part Removal
- Post Processing

The primary materials processed through a BAAM system are fiber reinforced polymer composites due to their lower coefficient of thermal expansion which reduces thermal warping and distortions during printing [33] Using fiber reinforced composites significantly reduces warping or distortions within the final printed component. These materials, fabricated via large area additive manufacturing, have successfully been implemented in various applications such as automotive tooling [34], molds for wind turbines [35], and boat molds [24].

2.6 Material Extrusion Build Parameters

The mechanical performance of a printed component is dependent on the specific build parameters used when slicing the standard tessellation language (STL) file and setting up the printer. The following sections cover the process control parameters that affect the geometrical and mechanical properties of both FDM and BAAM printed parts.

2.6.1 Extrusion Temperature

The temperature to which the monofilament or resin pellets are subjected during liquefaction in the hot end is referred to as the “extrusion temperature”. The molten material must be heated adequately to allow it to deposit through a nozzle and maintain a high enough viscosity for the bead to maintain its shape. As a rule, for most amorphous thermoplastic polymers, the greater the extrusion temperature the better the bond

between consecutive beads and layers. However, there is a trade off with the loss in dimensional accuracy of the final component. Balancing interlayer strength and dimensional accuracy is key to printing successfully.

2.6.2 Melt Flow Rate

The flow of plastic material that is being extruded from a liquefier head or element is known as the “melt flow rate”. FDM operates on similar principals as positive displacement pump to drive the monofilament through the orifice when the monofilament is being fed into the liquefier. This pumping approach subjects the process to greater sensitivity to the material feedstock. In other words, any slight variation in the monofilament diameter will directly affect the flow characteristics of the melt. A smaller diameter will result in a decrease in the melt flow rate which will lead to regions being unfilled in the printed part. Additionally, the use of a monofilament severely limits the deposition rates within FDM. Even if larger nozzles or orifices were used within the liquefier head, the nozzle must be smaller than the filament diameter to develop an adequate pressure for extrusion. Conversely, the BAAM printer uses a pellet fed single screw extruder, thus the pumping of the melt arises from a viscosity pump. Using a continuous pump allows for more precise control of the melt and allows for greater deposition rates. The combination of a larger nozzle (7-8 mm) and use of a screw extruder are what allow the BAAM printer to reach deposition rates as high as 36.3 kg/hour [31].

2.6.3 Printing Speed

The printing speed is directly related to the deposition rate or melt flow rate in each process. A component can only be printed as fast as that process is able to deposit material. As mentioned, FDM is limited in the rate it can extrude the plastic melt, thus printing at the printer’s maximum speed is not desirable as this results in an inconsistent extrusion flow. Inconsistent flow will lead to loss of dimensional accuracy and introduce defects into the printed part. Within FDM, printing at slower speeds is often desired due

to the reduced mechanical vibrations that are detrimental to part accuracy [36]. Parts produced using a BAAM printer can also be subjected to significant dimensional loss because of the increased deposition rate and the large bead width (8-9 mm). This is one of the reasons why current BAAM systems are equipped with a tamping device and undergo extensive post processing to correct dimensional accuracy [11].

2.6.4 Raster Orientation and Fill Density

When an STL file is prepared to determine the toolpath direction, the infill pattern of the raster is specified. The raster pattern for each layer ranges from 0° to 180° and can alternate between layers [37]. The most common raster infills, shown in Figure 2.5, are 0°, 90°, 45°, and alternating 45° & -45°. The direction of the raster or beads relative to the load direction greatly affects the mechanical performance of the printed component. Fill density represents the gap between consecutive beads within a given layer. A component with a larger fill density will exhibit improved mechanical properties compared to a part with a lower fill density.

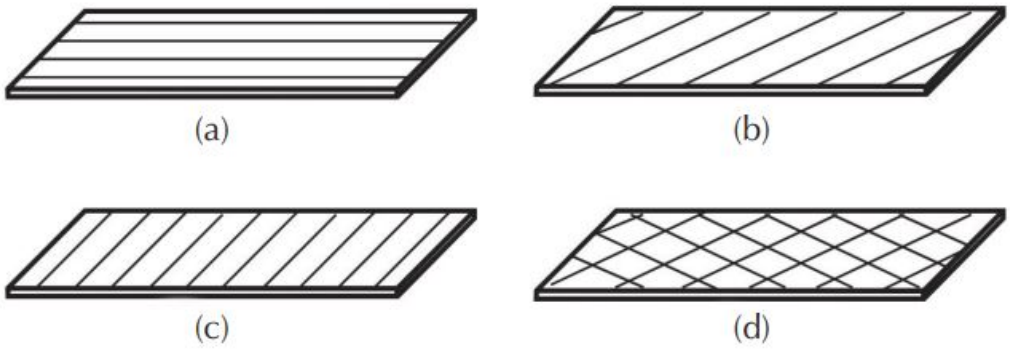

Figure 2.5: Different raster orientations used in 3D printing: 0° (a), 45° (b), 90° (c), 45° & -45° (d) [26]

2.6.5 Air Gap and Neck Growth

As alluded to in the previous section, the air gaps that form between deposited beads is a common feature of any material extrusion process. Figure 2.6 demonstrates

the various ways air gaps arise in each layer; between two raster beads, between two contour beads, and between a contour and raster bead. A sample printed at 100% fill, meaning there is no gap between adjacent beads, will still contain voids or air gaps among beads. Fabrication of a completely dense object in unachievable through AM material extrusion processes.

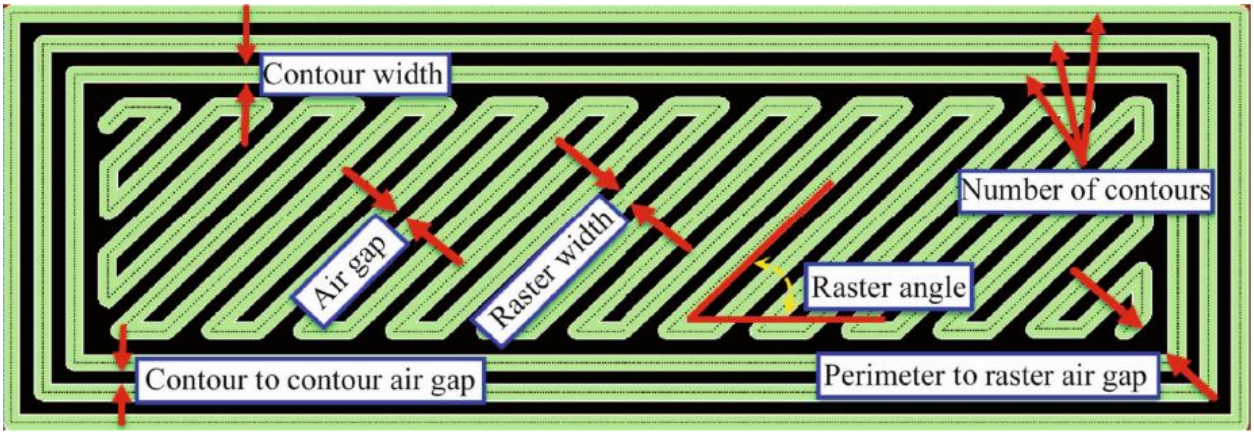

Figure 2.6: Illustration of the different air gaps formed in AM material extrusion [22]

The air gaps found inside a printed part act as stress concentrators, inhibiting the mechanical properties of the component. The gaps also provide an indication of the bond quality amid beads and layers. The quality of the bond formed among these beads is dependent on the growth of the neck formed between adjacent beads, molecular diffusion, and randomization of the bead surface [38]. Neck growth is determined by the surface tension, viscosity, and the heat transfer between the material and its surroundings [38], [39]. A model of the polymer bead neck growth is shown in Figure 2.7. Initiation of a neck occurs when two beads come in contact with one another (wetting) and diffuse together, forming an interfacial zone [38]. The size of the neck formation can estimate the level of bonding among deposited beads.

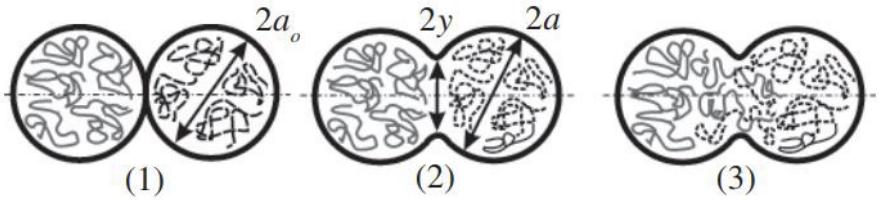

Figure 2.7: Model of the neck growth among two deposited beads [38]

Chapter 3: Mechanical Characterization of Large Area Additive Manufactured Components

In general, the field of AM suffers from a lack of specific test standards and methodologies for the mechanical testing of printed coupons. Examples in literature of the need for AM-specific test standards are ever growing. Despite efforts made to standardize test components for the dimensional accuracy of printed parts [5], [40]–[43], these attempts are insufficient. The need for AM-specific standards is exemplified by the work of Roberson, et al. [44], which pointed out that printing the notch for Izod impact testing of FDM-manufactured test coupons exposed raster pattern sensitivity of the impact strength while cutting the notch (as is the standard practice for polymeric parts) masked raster pattern sensitivity. Forster [45] also indicated the inadequacies of existing polymeric material test standards when applied to AM-produced test coupons.

When creating test coupons using large scale AM platforms, the size scale adds even more complication to the test coupon manufacturing process. The increased complication is because as the size of the beads and layers increase, so does the size of potential print defects. These defects, or voids, form due to the consecutive deposition of adjacent rows (beads) of material, typically 3.8 x 8.3 mm. This operation leads to printed objects not being fully dense. The existence of large bead size and corresponding print defects limits the usefulness of standards available for mechanical testing of polymeric materials, such as the ASTM D638-10 [46], because the size scale of the print bead approaches that of the test coupon dimensions. As an example, if an ASTM D638-10 Type III coupon was printed on a BAAM with a 7.62 mm nozzle the cross-section could have only a maximum of 5 beads, whereas, if you scale the tensile bar as demonstrated by Duty, et al. [11], you could fit up to 32 beads. Testing a greater number of beads instead of only measuring a localized area gives you more accurate results that are indicative of the true performance of the material and process combination.

3.1 Case Studies

There is no existing standard that addresses evaluating the mechanical properties of large-scale 3D printed parts. There is also a very limited amount of data reporting on these large, printed, composite parts. The study conducted by Duty, et al. [11] was able to describe the tensile strength of a wide variety of materials commonly processed through a BAAM printer. However, in the tensile test of the large coupons, strain measurements were not provided. The lack of strain measurements prevents the construction of stress as a function of strain diagrams, which is an essential criterion for material design. Recently, work done by Bedsole, et al. [47], reported the tensile strength and strain of acrylonitrile butadiene styrene (ABS) fiber reinforced composites processed through a BAAM printer. In the article, strain was measured by an axial extensometer with a 25.4 mm gage length on specimens with a gage length of 114.3 mm. No evidence is shown that the fracture occurred within the 25.4 mm of the extensometer used in that study. Although the strain measurement may still be valid for the determination of the elastic modulus at the early loading stage, it is not valid for determining the stress-strain curve, nor for the calculation of properties, such as chord and tangent modulus, which are of higher importance in materials with nonlinear responses such as polymers and composites. In addition to the size effect that might exist in the specimen, traditional instrumentation (clip extensometers) may be prohibitive toward large gauge lengths (greater than 100 mm). An alternative route to traditional instrumentation is the utilization of advanced non-contact instrumentation, such as digital image correlation (DIC).

3.2 Digital Image Correlation

Digital image correlation (DIC) consists of tracking visible features on the specimen in time-lapse monochromatic images, captured with digital cameras. These images of the deformed state are compared to the undeformed (original reference image) to provide full-field displacements and strains [48]. The DIC technique was first developed at the

University of South Carolina in the 1980 [49]. Since then the testing method has been refined to maximize accuracy and resolution within solid mechanics [49].

In the standard operation of a DIC, the tracking of a feature is achieved by comparing the change of grayscale levels at every n-number of pixels within each subset. Prior to capturing images, the DIC system must be calibrated by a grid of points with known separation for the system cameras to correlate a physical distance to a pixel distance and for the cameras to determine its spatial location.

Chapter 4: Experimental Procedures

In this study, BAAM printed fiber reinforced ABS composites were characterized to develop a broader understanding of the design criteria behind these components. The rheology of the ABS fiber composites was performed through a melt flow indexer (MFI). Test coupons were fabricated following the process described by Duty, et al. [11] to perform tensile testing on large printed coupons. Similar to the aforementioned process, tensile testing was performed on the BAAM-fabricated coupons and the methodology was expanded to include DIC to measure strain. DIC compares time-lapse photos to track displacements of visible features on the specimen; the features are either naturally occurring in the material, or more commonly, painted. To perform DIC strain measurement, a novel sample preparation process was developed to adequately add visible features to large specimens. A coating process established high-contrast speckle pattern on the specimens for the cameras on the DIC to track displacements of the speckles. Through the DIC data, Poisson's ratio was measured, and stress strain curves were plotted to determine elastic modulus. The critical fiber length was calculated and compared to the measured fiber lengths before and after the extrusion process. The critical fiber length was calculated as it is a critical characteristic to quantify the fiber/matrix interfacial debonding. Two neck growth studies were conducted to understand the effect of a large build surface and the variation of screw speeds.

4.1 Material Selection

The most common materials extruded by the BAAM system are fiber-reinforced polymers. These materials have enhanced mechanical properties due to the incorporation of short fibers into the polymer matrix. The material is reinforced by the stronger fibers transferring the load away from the softer polymeric material [17]. To maximize the reinforcement of the fibers within a polymer composite, it is necessary to have strong adhesion between the fiber and the matrix material [50]; therefore, preventing the fiber

from slipping during failure. Fiber reinforced polymers are commonly used in the aerospace, construction and medical industries [51]. With respect to BAAM printed components, these materials have been used for automotive tooling and large structure molds [24], [35], [42].

The work performed in this study focuses primarily on fiber-reinforced ABS composites due to the ease of processing these composite blends through a single screw extruder and the superior mechanical properties compared to neat or pure ABS, specifically high strength, stiffness, and fracture toughness [52]. Additionally, amid the available materials designed for BAAM printers, fiber-reinforced ABS blends are relatively inexpensive as these materials are categorized as low temperature amorphous polymers. For the analysis described in this thesis, a glass fiber-loaded (20 wt.%) ABS composite (HiFill J-1200 20GF, Techmer PM, Clinton Tennessee, USA) and a carbon fiber-loaded (20 wt.%) ABS composite (ElectraFill J-1200 20CF, Techmer PM, Clinton Tennessee, USA) were acquired. As the primary focus of the study is to contribute to the characterization of BAAM printed components to establish design parameters for multi-process AM of electrical components, an electrical study was carried out.

4.1.1 Electrical Study

The purpose of conducting an electrical/resistance study was to determine if the filler content in the composite blend would present a risk of an electrical short when the material was subjected to a wire embedding process. The study was designed specifically for the ABS-20CF blend due to the conductivity of the carbon fibers themselves, thus the bulk resistance is investigated.

From a spare test block of the ABS-20CF printed on a Cincinnati BAAM – 100 system (Cincinnati Incorporated, Harrison, Ohio, USA) a 50 X 15 X 10 mm rectangular block was harvested. It is Important to note that the print settings used to fabricate the block were not recorded as the purpose of this study was to gather insight on the risk of

an electrical short. The ABS-20CF coupon was embedded with four 32-gauge wires with a 1 mm spacing between each wire, as shown in Figure 4.1a.

The embedded coupon was connected to a power supply to pass a current through two adjacent wires, to create a bias between the wires and power supply. Current was applied for a five-minute interval, then paused to measure the resistance of each wire, the resistance between the two wires, and the composite block itself. Figure 4.1b shows an illustration of how the resistance was measured among two wires. The current was incrementally increased until a short (if any) occurred. The results of the electrical test are shown in Table 4.1. From the table, there is a clear flow of electrical current from one wire to the other. The resistance recorded between each wire, regardless of where the measurement was made on each of the wires, showed to be around 13 ohms. The presence of a resistance validates the concerns regarding crosstalk between electrical components. When the ABS-20GF composite was tested, resistance measurements of the block and between adjacent wires showed to not have any readings. Meaning the issue of crosstalk is not present with the glass fiber composite, a characteristic that was predictable. Subsequently, an ABS blend loaded with 20 wt.% carbon fiber is not an ideal material choice to use for wire embedding applications. Due to these risks, the focus of this paper was concentrated on the ABS-20GF blend.

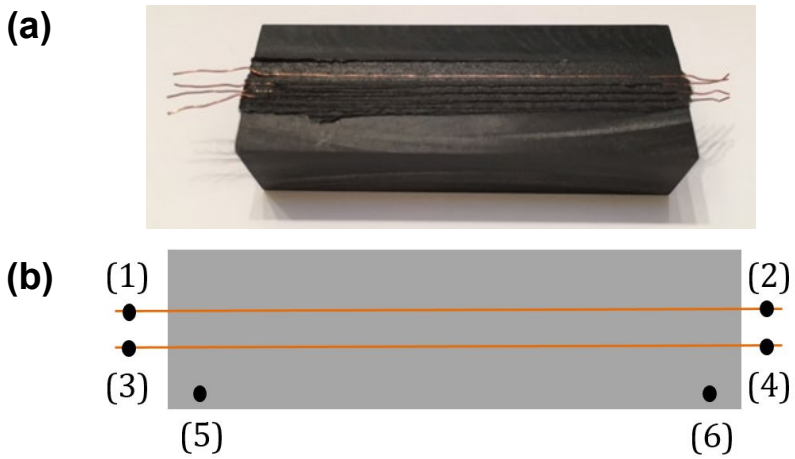

Figure 4.1: Image of the wire embedded block (a) reference image where resistance measurements we taken (b)

Table 4.1: Measured resistance of the ABS-20%CF block at different currents, see Figure 4.1 for measurement reference

Current	Voltage	Resist-ance from 1-2	Resistance from 1-3	Resistance from 1-4	Resistanc e from 2-3	Resistance from 2-4	Resistance from 3-4	Resistance of composite block from 5-6
(A)	(V)	(Ω)	(Ω)	(Ω)	(Ω)	(Ω)	(Ω)	(KΩ)
0	0	0.0855	13.687	13.346	13.270	13.096	0.082	0.595
1	0.187	0.0815	13.148	13.261	13.149	13.066	0.081	0.519
2	0.723	0.0780	13.225	13.201	13.140	13.202	0.080	0.551
3	0.690	0.0795	13.192	13.720	13.120	13.175	0.081	0.575
4	0.902	0.0796	13.234	13.431	13.169	13.180	0.077	0.543

4.2 BAAM Extrusion Parameters

Despite this study's main intention to further characterize an ABS-20GF composite blend processed through a BAAM extruder, an ABS-20CF resin was also used due to a limited amount of material. Prior to processing, the ABS fiber reinforced pellets were dried in a compressed air dryer (Dri-Air HPD Series, East Windsor, Connecticut, USA) at 82°C for 4 hours. Test structures were processed using a Cincinnati BAAM – 100 system with a 7.62 mm extrusion orifice. The BAAM – 100 system was furthermore equipped with a reciprocating tamper mechanism. The specific barrel temperature zones were selected to ensure that the top layer maintained a temperature above the glass transition temperature (Tg) of the composite, prior to the next layer being deposited. Compton, et al. [53] reported that maintaining a top layer greater than the Tg of an ABS and carbon

fiber composite prevented rapid cracking and warping on the final component. Applying those principals with our blends and using the resin manufacturer's specifications, the extrusion settings were identified, see Table 4.2. The only modification made was with respect to the screw speed for the ABS-20CF blend, as alternating screw speeds and its effect on neck growth were analyzed.

Table 4.2: BAAM parameters for glass fiber and carbon fiber ABS.

	T Melt (°C)	T Barrel 1 (°C)	T Barrel 2 (°C)	T Barrel 3 (°C)	T Barrel 4 (°C)	T Tip 1 (°C)	T Tip 2 (°C)	Pump Speed (rpm)
ABS-20GF	215	215	220	230	225	220	215	55
ABS-20CF	225	200	215	240	240	230	225	50-400

4.3 RHEOLOGY

The rheology of the ABS with 20 wt.% glass fiber pellets was performed on a Tinius Olsen MP1200 melt flow indexer (Tinius Olsen, Horsham, Pennsylvania, USA) (Figure 4.2) following the ASTM D1238-13 standard [54] (procedure A, ASTM International 2013). Prior to testing the ABS-20GF pellets were dried using a compressed air dryer (Dri-Air CFAM Micro-Dryer, East Windsor, Connecticut, USA) at a temperature of 82°C for a period 4 hours. MFI was also conducted on various polymer blends, commonly used in large scale extrusion, for comparison. All tests were conducted using the same machine-operating parameters: a temperature of 230°C and a 3.8 kg test load.

Figure 4.2: Tinius Olsen MP1200 Melt Flow Indexer

4.4 Critical Fiber Length

Samples of the ABS-20GF composite material were collected before and after extrusion, to use for fiber length analysis. Glass fibers were extracted from the polymer matrix through the process of pyrolysis, which involves the thermal degradation of the polymer. Pyrolysis was carried out by placing the composite material in an oven at 600°C for approximately 30 min, as described by Ozkoc, et al. [55]. The ash remnants were collected in a 60 mm petri dish and mixed with deionized water. Fibers were analyzed using a Keyence VHX-6000 Digital Microscope (Keyence, Osaka, Japan) to determine fiber length before and after processing. A minimum of 18 images were taken and image analysis was conducted using ImageJ.

4.5 Single Bead Characterization

Glass fiber orientation and skin effect [11] within the ABS matrix are analyzed for an extruded bead sample. Bead samples of the ABS-20GF were collected from the BAAM pellet-fed single screw extruder following the parameters described in Table 4.2. These samples were sectioned and mounted for metallographic-like polishing. Mounted samples were polished using 240-4000 grit silicon carbide papers to reveal the vertical cross-

section and the horizontal cross-section of the bead, see in Figure 4.3. The as polished samples were viewed on a Hitachi SU3500 variable pressure SEM (Hitachi America, Ltd, Tarrytown, NY, USA) operating at 10 kV accelerating potential and with a backscatter electron detector (BSE) in a 70 Pa vacuum.

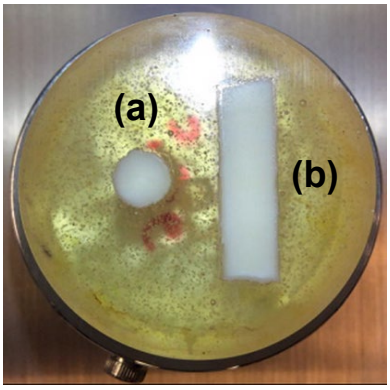

Figure 4.3: Mounted and polished single bead showing the vertical cross section (a) the horizontal cross section (b)

4.6 TENSILE SPECIMENS

Following the design described in the report by Duty, et al. [11], a hexagon was printed with a 3.81 mm layer height and a bead width of 8.33 mm. The large hexagon measured to be 70cm long on each side, 17cm tall, and 2.5 cm thick. To reduce the air gap caused by the deposition of sequential beads, the hexagon was printed with 100% fill and 3 contours. The parameters mentioned in Table 4.2 are the same settings used on each contour and layer. Using the manufacturer's extrusion recommendations, the ABS-20GF hexagon printed successfully and showed no indications of warping or distortions. Tensile test coupons were then harvested from the large hexagon by initially sectioning the structure at each corner. Figure 4.4 demonstrates the exact location each specimen was sectioned relative to one another (red circle indicates contour seam).

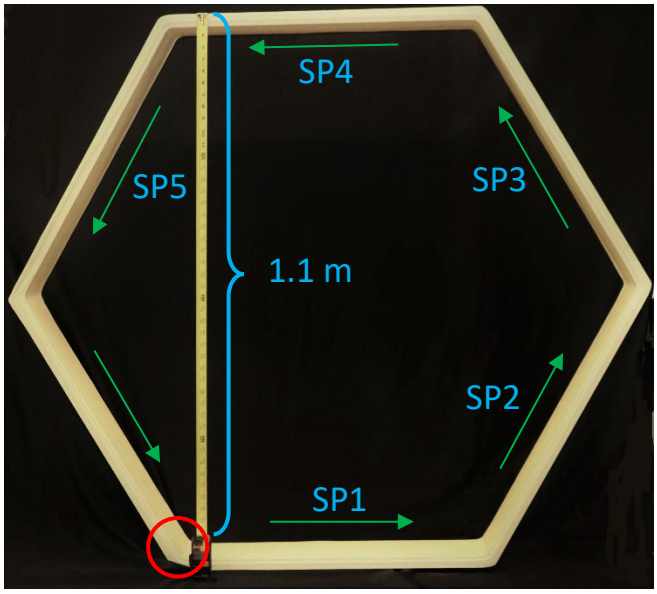

Figure 4.4: Image of the printed hexagon showing the location of each specimen, green arrows indicate build direction, and red circle specifies seam edge

Five of the panels were then milled flat by removing equal amounts of material from both sides. A single modified ASTM D638-10 Type I [46] coupon was then sectioned from each panel (Figure 12). The coupon was machined so that the primary axis (longest side) was in the same direction as the toolpath, following the green arrows in Figure 11. Two gage marks were placed on each specimen, spaced 127 mm apart from each other, to represent the straight region on the coupon.

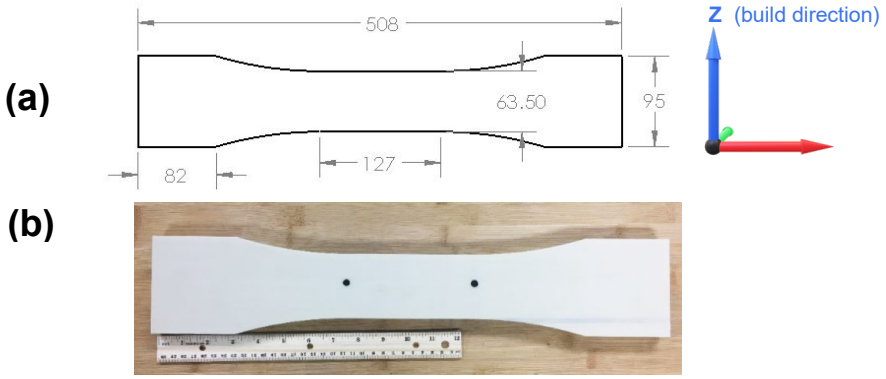

Figure 4.5: Large tensile specimen dimensions (mm), thickness of 19 mm (a) Image of harvested tensile specimen (b)

4.7 TENSILE TEST

Tensile testing was performed using a modified version of ASTM D638-10 [46] with variation in specimen dimension and strain rate. Large flat tensile samples were conditioned following the ASTM D618-13 (Method B) [56], for 48 hours at 50°C then placed in a desiccator for an additional 15 hours. Samples were tested using an MTS Landmark 370 servo-hydraulic system (MTS, Eden Prairie, Minnesota, USA) equipped with a 647.10 hydraulic wedge grips and a 100 kN load cell. Due to the large specimen size (thickness of 19 mm), custom 4-inch wide wedge plates with a 17 mm to 25.4 mm opening, were manufactured for the 647.10 hydraulic grip. To produce results comparable to the work performed by Duty, et al. [11], the testing speed was controlled by a constant cross head speed of 0.025 mm/s and at a temperature of 23°C, until rupture. In addition, a Correlated Solutions 3D image correlation system (Correlated Solutions, Irmo, South Carolina, USA) was used for strain measurements (Figure 4.6).

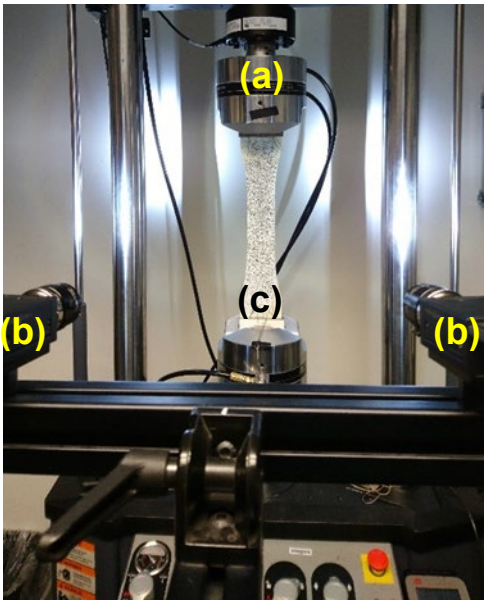

Figure 4.6: Specimen with optical instrumentation setup (a) grips, (b) cameras, and (c) specimen.

As the DIC system optically tracks the displacement of visible features, it was necessary to prepare the flat specimens prior to testing. In DIC, a reference image (typically the first of the time lapse) is divided into subsets, containing speckles, which are

tracked as the specimen deforms. The tracking consists in shifting subsets in the deformed image until the speckle pattern matches the reference image as closely as possible; this match is calculated as the total difference in gray levels at each point. As no highly visible features were initially present on the specimens, a speckle pattern was applied to the specimens. First a flat-white base coat was uniformly applied using Rustoleum Ultra Cover Paint+Primer and, immediately after, 1mm black crafting glitter (Horizon Group USA) was randomly applied, on the gage length only, with a shaker and deposited by gravity on the fresh white paint at a dose of approximately 67 mg/cm^2, which is equivalent to 5 grams of glitter per specimen. Finally, a layer of Rustoleum Ultra Cover Matte Clear was applied, fading the sparkling effect from light applied to the specimens during testing (Figure 4.7a). This procedure was found to produce specimens with acceptable speckle patterns in terms of density, contrast, random distribution and speckle size distribution, which resulted in consistent correlation of images (Figure 4.7b)

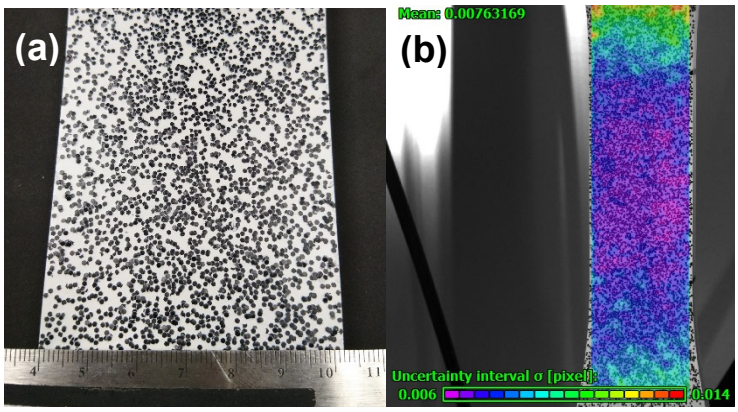

Figure 4.7: (a) Speckle pattern applied on the tensile test specimen. (b) Uncertainty in the correlation of subsets in images

The specimens were then installed and aligned using a bubble level and MTS wide wedge grips. For strain measurements, the DIC system was setup and calibrated following Correlated Solutions' recommendation for stereoscopic images using 17 mm lenses (Xenoplan 1.4/17-0903) and two Flir Grasshopper 1394b 2MP monochrome

cameras (GRAS-20S4M-C). For the determination of a measured stress-strain curve of the material, the DIC and the testing frame were synchronized to record data points at 0.5 s intervals to compare the applied stress and recorded strain at the same time.

4.8 Fractography

Fractography was taken using macro digital photography and SEM. For the macro digital photography, a Nikon D5100 camera was used with 40mm f/2.8G macro lens. Electron characterization of the fracture surface was performed using a VP-SEM operating at 10 kV with an UVD in a 70 Pa vacuum. Polymer composites were sputter coated with gold to provide conductive surfaces using a JEOL smart coater (JEOL USA, Peabody, MA, USA).

4.9 Neck Growth Variation between ABS-20GF Tensile Samples

The remaining unused segments of panel 2 and 5, from the ABS-20GF hexagon (Figure 1), were both sectioned cross-sectionally at identical locations to reveal their contours. Specimens were then finished with 4000 girt silicon carbide polish and viewed on a VP-SEM (Hitachi SU 3500) operating at 10 kV accelerating potential with a BSE in a 70 Pa vacuum, to analyze the necks formed between beads. Image processing via ImageJ, was conducted to measure the size of each neck between contour (i) and (ii) as depicted in Figure 4.8. The neck size was measured for layers 16 through 27, which constitutes as the centermost region of the hexagon walls.

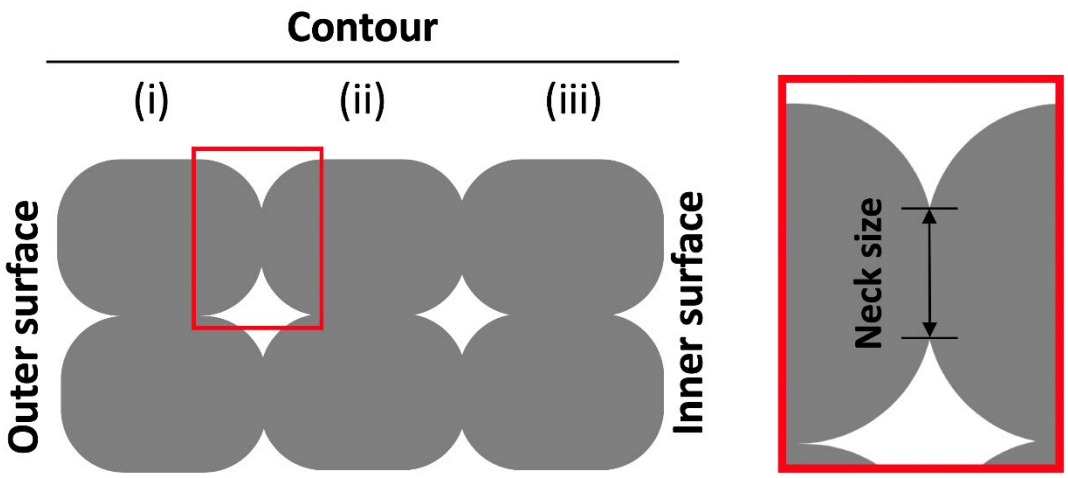

Figure 4.8: Illustration of where the neck size measurement we taken

4.10 Neck Growth and Screw Speed Relationship

An additional neck growth study was conducted that considered variations in the extrusion process, concentrating exclusively on the screw speed in the BAAM extruder. Due to the limited quantity of ABS-20GF pellets available, the ABS-20CF blend was used for this investigation to determine which screw speeds provided a consistent flow of material that was free of any porosity. Bead samples of the ABS-20GF extruded at 5 different screw speeds (50, 150, 250, 350, 400 rpms) were collected. Samples were mounted and polished in the same manner as those in Figure 4.3(a) with a 4000 grit silicon carbide polish to reveal the vertical cross sections of the beads. Polished surfaces were viewed on the VP-SEM mentioned above, operating at a 10 kV accelerating potential with a BSE in a 90 Pa vacuum.

The screw speeds that maintained a consistent bead cross section, free of significant defects were selected for the final neck growth study. Trapezoidal structures were printed on the BAAM – 100 system with a 3.81 mm layer height and a bead width of 8.33 mm at different screw speeds. The dimension of the small trapezoidal structures is shown in Figure 4.9 printed with 100% fill and 3 contours.

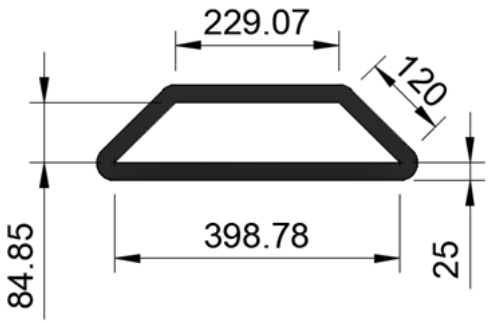

Figure 4.9: Dimensions (mm) of the trapezoidal test structure, thickness was 4 layer or 15.24 mm

On the center of the longest base for each structure, three 25 mm specimens were machined. Sectioning was performed in a transversal manner to reveal the contours on each specimen, see Figure 4.10. The polished specimen surfaces were examined using VP-SEM with an accelerating potential and vacuum settings of 10 kV and 90 Pa, respectively, in the same manner as described to section 4.8. Image processing, via ImageJ, was conducted to measure the size of each neck between contour (i) and (ii) as well as between contour (ii) and (iii) as depicted in Figure 4.8.

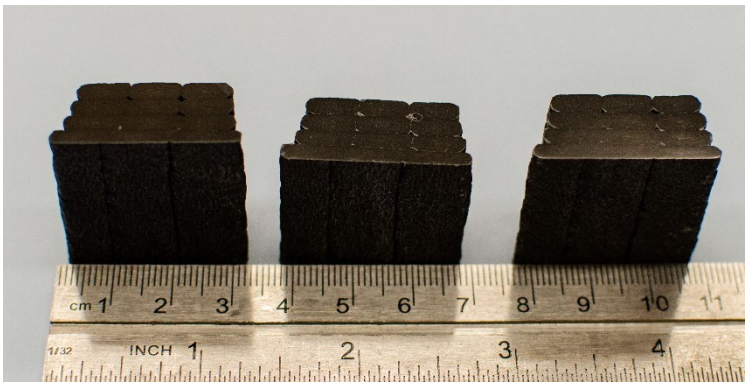

Figure 4.10: Image of the cross sectioned ABS-20CF samples used to measure neck formations

Chapter 5: Results and Discussion

5.1 Rheological Results

MFI was conducted on two fiber-reinforced ABS blends and a neat ABS (MG94) for comparison. ABS MG94 is the most widely used extrusion grade ABS in desktop 3D printing [57]. The results of the MFI measurement are tabulated in Table 5.1. The melt flow of the ABS-20GF (1.74 g/10 min) and the ABS-20CF (1.18 g/10 min) are considerably lower than the measured value of neat ABS (14.83 g/10 min), indicating viscosity during extrusion will be higher for the composites. Moreover, the MFI measurements among the two 20 wt.% loaded fibers are quite similar with one another, suggesting that their extrusion process parameters will be alike.

Table 5.1: Melt Flow Index Results

Material	Measured MFI (g/10 min)
ABS-20GF	1.74
ABS-20CF	1.18
ABS MG94	14.83

5.2 ABS-20GF Single Bead Characterization

In the article by Duty et al. [11], the authors commented that as a result of extruding a fiber reinforced composite through a large orifice, the bead experienced a “fiber skin” of highly oriented fibers on the bead edge. The purpose of conducting the single bead analysis was to determine if our BAAM printing parameters would experience a similar effect. SEM images of the ABS-20GF bead cross sections are shown in Figure 5.1. Inspection of the vertical cross-section does not provide any indication of a dense concentration of highly oriented glass fibers towards the bead edges. Instead, majority of the fibers throughout the cross section appeared to be distributed evenly throughout the bead. In the horizontal cross section of the bead, the glass fibers closest to the bead

surface do show a preferential alignment with the direction of material flow. The farther away from the edge, the fibers appear more randomly oriented within the bead. Through the given processing parameters for ABS-20GF, fibers have a mixed orientation mode with alignment on the bead edges.

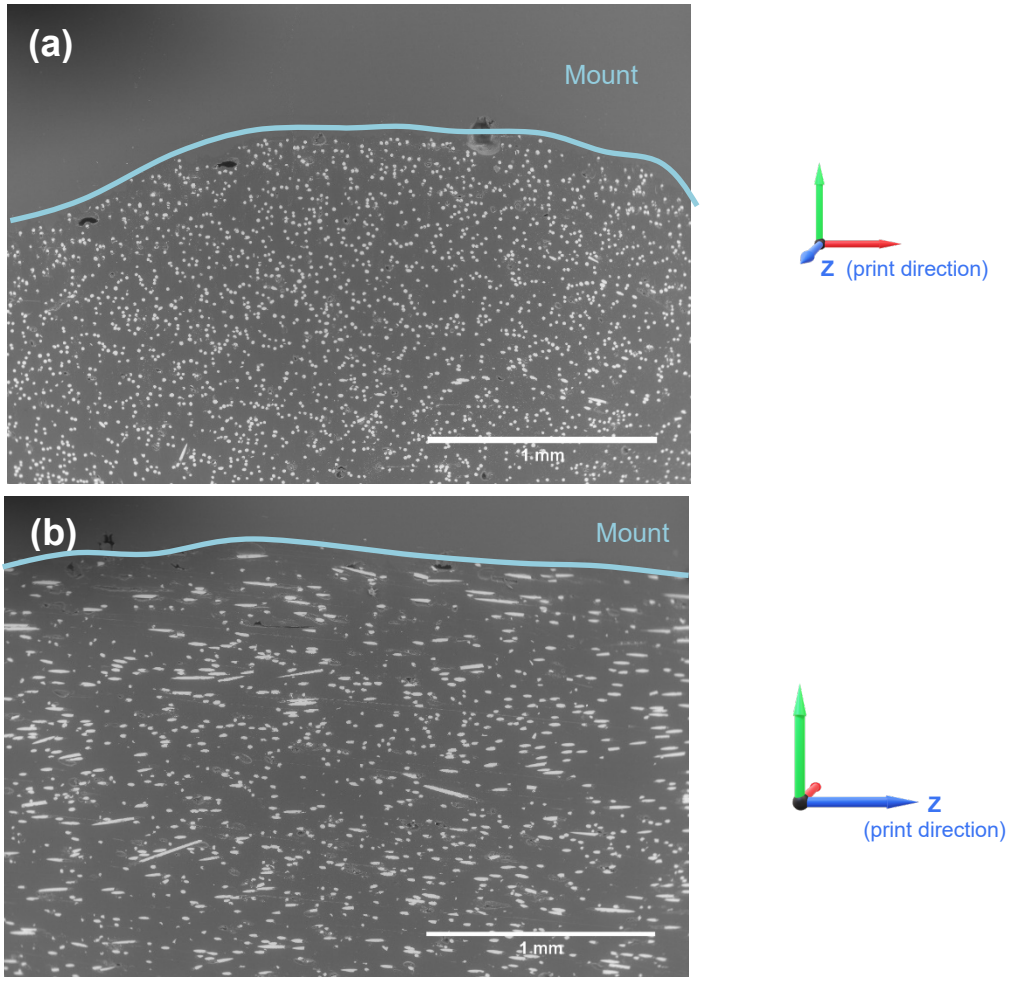

Figure 5.1: SEM images of the ABS-20GF single bead, vertical cross section (a) horizontal cross section (b)

5.3 Tensile Results

The DIC was used to obtain the elastic modulus, Poisson's ratio, and local longitudinal strain of the composite material. The DIC system used a reference image taken at (t = 0 sec) that was compared to new images taken as the tensile test proceeds and final rupture occurs. The displacement of the black specks on the sample surface is

measured and thus, strain fields are generated for the material. In addition, longitudinal and transverse virtual extensometers were placed on the images during post-processing, using the VIC-3D software, to calculate the local longitudinal strain. The experimental tensile test results on the large flat specimens are presented in Table 5.2. Refer to Figure 4.4 for the specific location of each sample on the hexagon. The average ultimate tensile strength, in the direction of the toolpath, was 52.84 MPa ±0.70. Despite the limited sample pool size, the maximum stress reached by each specimen was highly consistent to one another. When compared to similar ABS-20GF specimens tested in the same manner there was a 14.46 MPa decrease in the ultimate tensile strength in our samples. This discrepancy can arise from many factors related to the BAAM system. First, the BAAM used in this study is different than the one mentioned by Duty, et al. [11], meaning that the extrusion screws used were different as well. Additionally, the barrel zone temperatures and screw speeds may not have been optimized for the hexagonal structure.

Table 5.2: Mechanical properties of the ABS-20GF coupons.

Property	BAAM					Duty, et al. [11]
	SP1	SP2	SP3	SP4	SP5	
Ultimate Tensile Strength, MPa	52.11	52.59	53.85	52.17	53.48	67.3
Elastic Modulus, GPa	5.806	5.406	5.368	5.365	5.375	
Poisson Ratio	0.361	0.351	0.347	0.376	0.319	

Our study demonstrated consistency among the machined tensile specimens with a coefficient variation (CV) of 0.01 for the tensile strength. These results are significant since the samples were harvested from different sides on a large hexagon, meaning that specimen 2 (SP2) and specimen 5 (SP5) were printed approximately 1.2 m away from

each other. At first glance the larger build volume was projected to present a greater risk of inconsistent envelope temperatures at different regions of the build platform. Fortunately, the small tensile strength CV suggested that the extent of bonding among layers was uniform throughout the BAAM – 100 build platform. Inconsistencies (if any) with the envelope temperature had no profound effect on the tensile properties.

The stress-strain curves for the ABS-20GF composites are plotted in Figure 5.2. From the plot, it is quite clear how comparable the stress-strain curves are to one another. Each specimen experienced linear elastic deformation up to 0.005 mm/mm and 30 MPa stress. Beyond a strain of 0.005 mm/mm, the material experienced limited plastic deformation based of the parabolic shape of the curve. The limitation of a plastic region complies to what is typically found among fiber reinforced polymers that exhibit a high modulus and tensile strength. The modulus of the composite material was determined by calculating the slope (stress/strain ratio) of the elastic region and was observed to be within 5.37 to 5.81 GPa. The Poisson's ratio of the coupons was measured using the DIC data collected from the longitudinal and transverse installed virtual extensometers. Poisson's ratio was found to be within 0.3 to 0.38 for the ABS-20GF composite blend. Knowing the elastic modulus and Poisson's ratio is fundamental in characterizing and establishing design limitations on this large additively manufactured composite components.

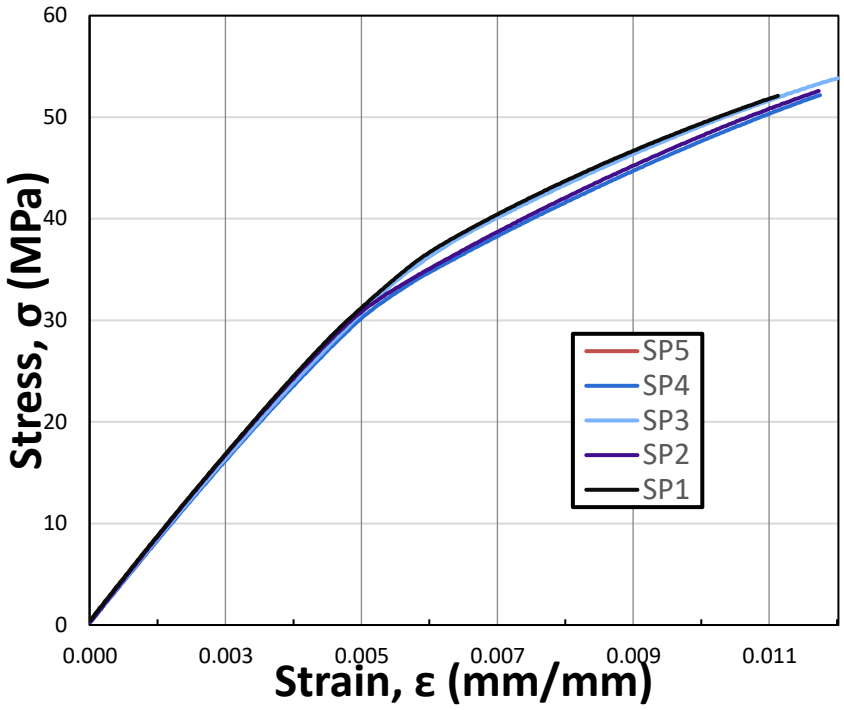

Figure 5.2: ABS-20GF Stress-Strain Curves

Only one coupon, specimen 5 (SP5), from the sample pool fractured within the 127 mm-gage length. SP5 results could have invalidated the testing of the other specimens if traditional instrumentation, such as clip extensometers or strain gauges, were used. In DIC, regions of interest can be defined on images; thus, knowing from the images where the fracture occurred, the virtual extensometers were set for elongation measurements on this area of interest to obtain the stress/strain data from the rupture region (Figure 5.3). Specimens were analyzed to observe the von Mises (VM), principal, normal, and shear strain fields at the midpoint of the tensile test (Figure 5.4). The DIC data, taken at that exact frame, represents the apparent elastic loading condition for the ABS-20GF specimen. For SP5, the principal strain E1 exhibits a maximum strain of 6.94e-3 at the upper left region (red region in Figure 5.4(ii)) of the sample. The principal strain E1 coincides with the strain field εyy, measured to be 6.91e-3 at the identical location (red region in Figure 5.4(vi)). The similarities among E1 and εyy suggest that the material is experiencing minimal shear effects and is primarily dependent on εyy. Results are a

typical observation from a symmetric specimen loaded parallel to the layers orientation and was consistent among all samples. The exclusion of shear occurring is further supported when comparing the strains measured in the center of the specimen in E1 and εxx, -2.29e-3 and -2.25e-3 respectively (Figure 5.4(iii,iv)). In addition, the similarities among the principal strains (E1, E2) with the strain fields (εyy, εxx) demonstrates that the material is under a triaxial stress state (σ_{yy}, σ_{xx}, σ_{zz}). When comparing these findings with previously reported DIC measurements on FDM printed parts [58], axial strain field distributions for BAAM and FDM samples printed with a 0° raster angle (raters and layers are fabricated parallel to the axial load) are comparable. In both cases strain fields were uniform in the horizontal direction and exhibited high strain concentrations on the outer edge of the specimen. The related strain field distribution among the FDM and BAAM printed components suggest that the small-scale experimentation with FDM does provide a reasonable prediction of how a much larger scale BAAM specimen might behave under an axial load. However, the work presented here only considers a single contour direction without accounting for variation of the air gap formed during sequential bead deposition. To better establish the connection among FDM and BAAM printed components these parameters must be investigated.

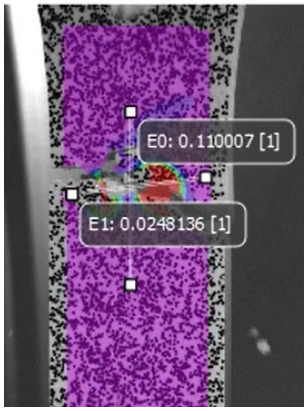

Figure 5.3: Virtual extensometers placed on the fracture site

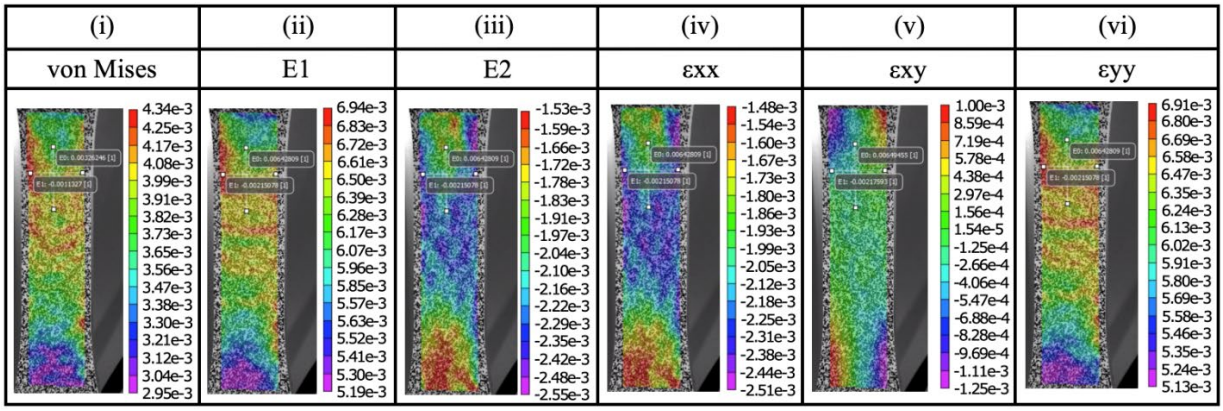

Figure 5.4: DIC strain fields of the ABS-20GF specimen at the midpoint of the tensile test

SP5 was further analyzed to visually observe the von Mises (VM), ε_{XY}, and ε_{YY} strain fields at the onset of final failure (Figure 5.5). Strain fields in the ε_{YY} and VM are nearly identical to each other indicating that fracture was primarily dependent on the ε_{YY} only. This observation further supports that the material is under a triaxial stress state (σ_{yy}, σ_{xx}, σ_{zz}) with minimal shear effects. As noted in the apparent elastic loading condition, the maximum strain on SP5, occurred at the upper left region (red region in Figure 5.5(i)) which can be marked as the necking region. The specimen ultimately failed in this highly strained region as depicted in Figure 5.5(iv), further confirming the DIC measurements.

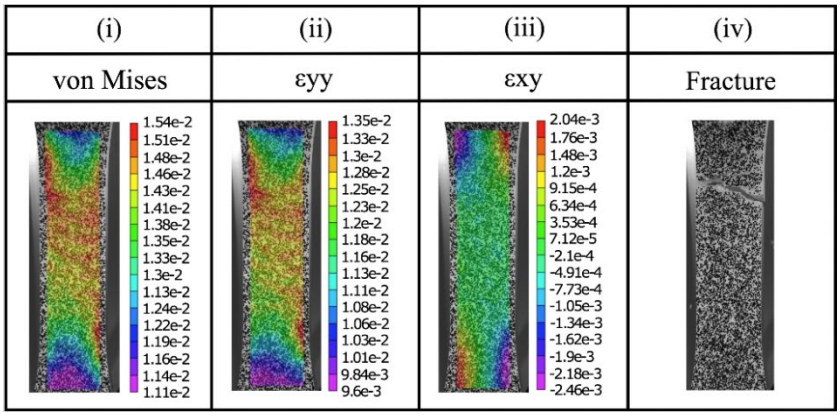

Figure 5.5: DIC strain fields on ABS-20GF specimens at an instant before rupture

5.4 FRACTOGRAPHY

Photographs of the fracture surface were taken for two specimens (SP4 & SP5) and are displayed in Figure 5.6. The fracture behavior was consistent with craze cracking. It is notable that the strain fields in Figure 5.5 are roughly at a 45° angle. The strain field correlates well with the observed fractographic evidence as the physical sample indicates that crack initiation started on the left side of the specimen and propagated inward. The site where these cracks extend out (see Figure 5.6(b), red arrows) is indicative of a cleavage stop [59] where crack propagation was altered due to an inhomogeneous defect causing branching of the crack. Secondary cracking, parallel to the applied stress, in the 45° direction followed. This secondary crack propagation was driven by shear forces and initiated at this cleavage stop. The final rupture occurred at the right side of the specimen where a tear-like feature is observed on the specimen surface in Figure 5.6(c). The image in Figure 5.6(d) (red arrow) shows that these crack initiation sites stem from the printing-related defects caused by the sequential deposition of material. These voids act as stress concentrators when pulled by an axial load. Another observation is how different the printing gaps are from one contour to another. Figure 5.6(b) shows the variation of the gap size; the edge with the larger gaps represents the outer surface of the hexagon. Variation of the raster gap sizes signifies issues related to the slicing of the original CAD model.

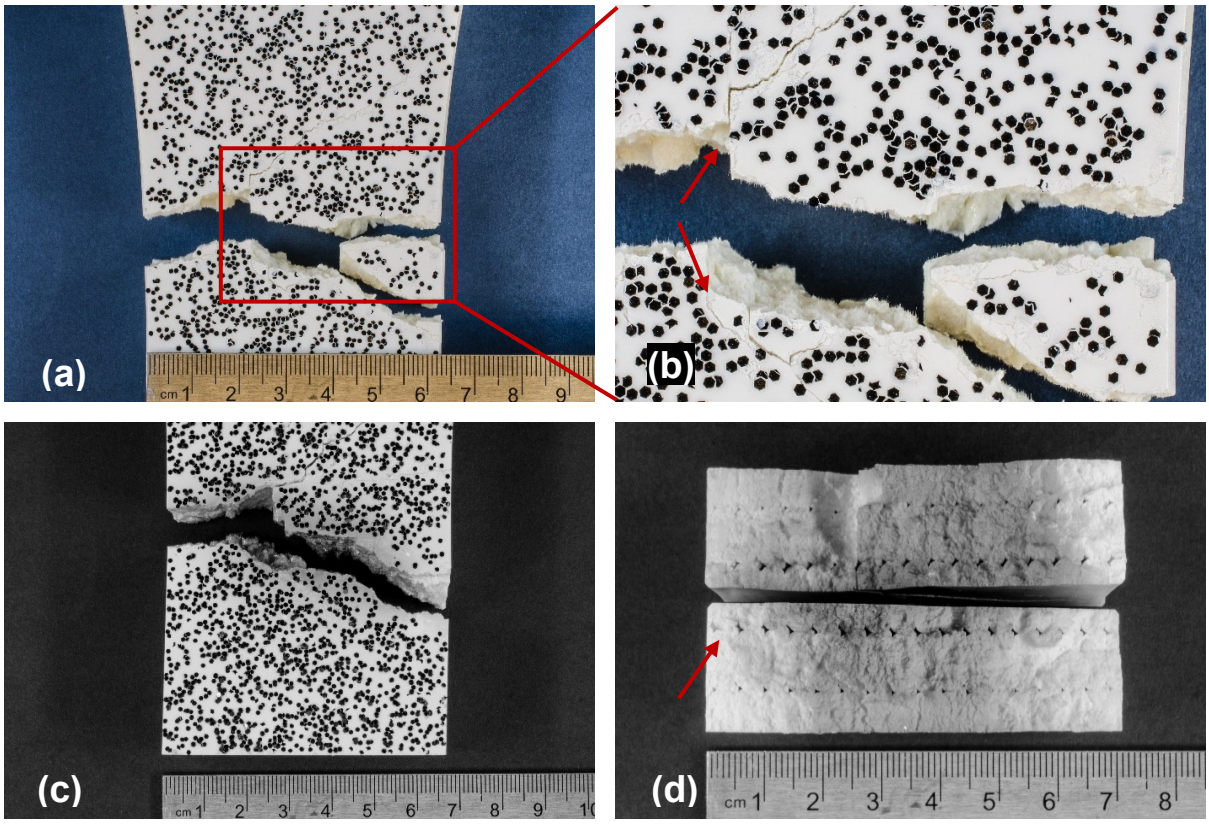

Figure 5.6: Fracture surface images of the tensile specimens (a,b) crack initiation site for tensile sample 4, (c,d) tensile sample 5

SEM images of the fracture surface were taken from sample 5, as this was the only specimen to rupture within the drawn gages, Figure 5.7. The void developed during processing was found to have a cross-sectional area of 0.82-mm^2. The fracture surfaces in Figure 5.7(c,d) exhibit brittle fracture characteristics due to the flake morphology present. In addition, the surface contains circular dimple cavities with diameters ranging from 40 to 70 μm. These cusps are indicative of opened faces of circular craze cracks and have been observed on the fracture surface of ABS reinforced with jute fiber tensile specimens [60] that displayed brittle fracture characteristics. Moving away from the raster gap void and studying the bond between two distinct layers there is evidence of added print-related defects, see Figure 5.8. The 3 voids are found in the interface between the two layers, representing poor adhesion between layers. Looking solely at the glass fibers in this micrograph, the fibers have a mixed orientation.

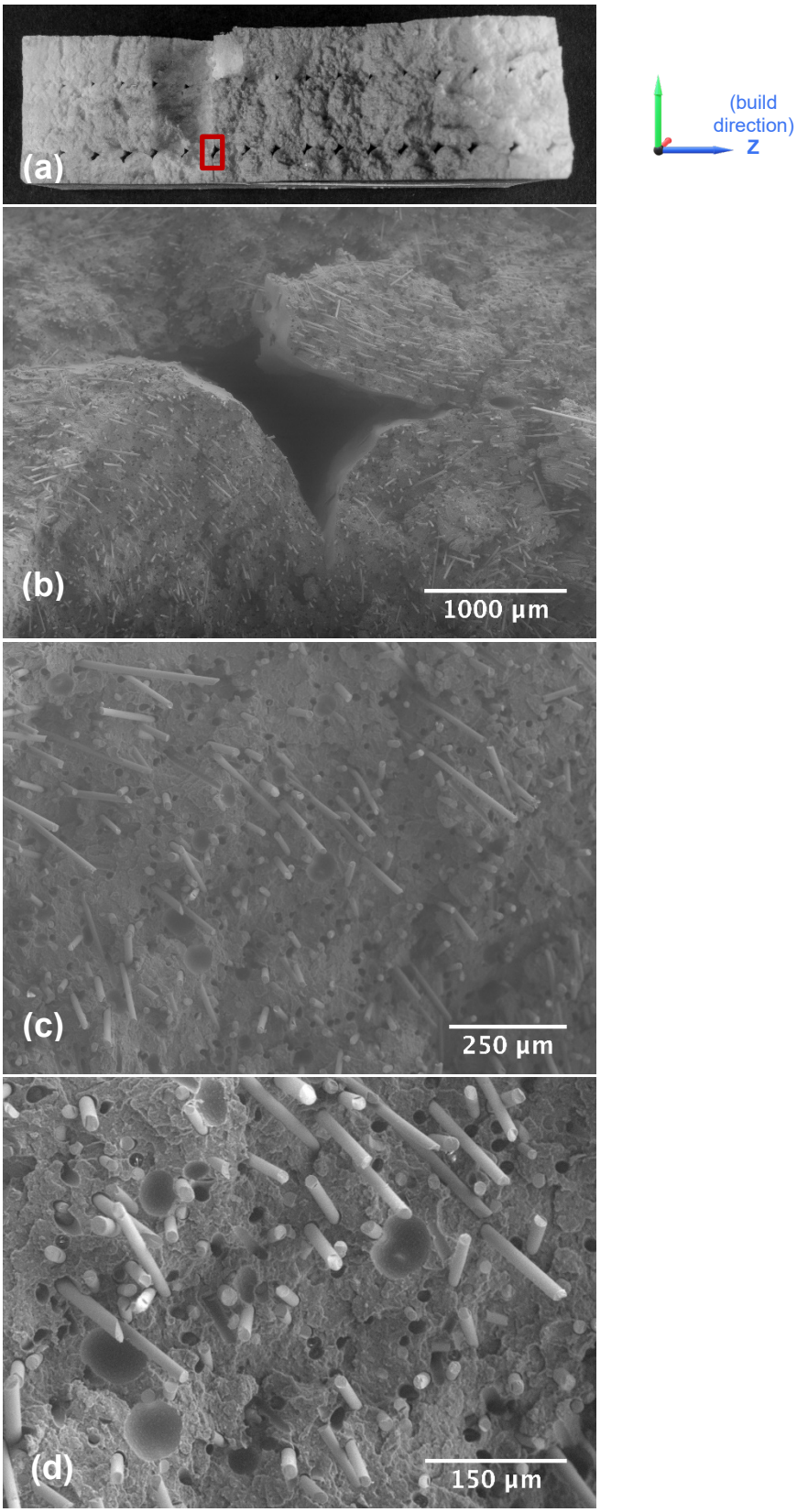

Figure 5.7: Images of fracture surface of sample 5, (a) photograph of a print gap, (b-d) SEM images of the fracture surface.

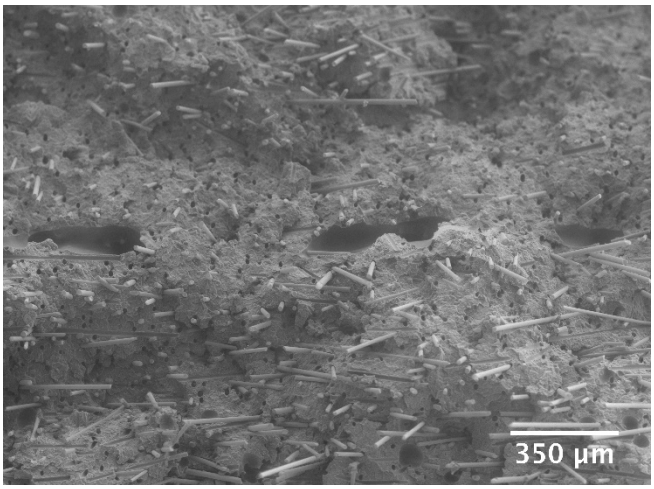

Figure 5.8: SEM image of the bond between two layers.

Another imperative feature that is observable throughout the ABS-20GF microstructure is the lack of fibrils among the fiber/matrix interface. This suggests that the bonding between the glass fibers and the polymer matrix is poor and debonding and gliding can readily occur under a load. Looking at the voids left behind from fiber pull out, shown in Figure 5.7(d), further supports this notion. The evidence of poor adhesion from fiber pullout denotes that the material will exhibit a lower strength. This surface analysis complies with the results found in stress-strain curves, where lower ultimate tensile strengths were reported, and a brittle failure mode dominated these specimens. The lack of adhesion of the filler material will also cause the interface between fiber and matrix to act as a secondary crack initiation site.

5.5 Critical Fiber Length

Through the failure analysis of the ABS-20GF tensile specimens, it was determined that the cause of the low reported tensile strength was due to poor adhesion between the fiber and matrix. To quantifiably assess that the glass fibers will pull out of the polymer matrix rather than fracture, the glass fiber lengths were measured and compared to the critical fiber lengths. The critical fiber length (l_c) of the ABS-20GF blend was calculated based of the following equation [61]

$$l_c = \frac{r_f \sigma_{fu}}{\hat{\tau}} \quad (1)$$

where (r_f) is the radius of the fiber, (σ_{fu}) is the fiber strength, and ($\hat{\tau}$) is the interfacial strength of the composite [61]. As provided by the manufacturer, the fiber radius is 7.5 μm with a strength ranging from 3000 to 3500 MPa. An interfacial strength of 23.5 MPa was used in this calculation as measured by Pisanova, et al. [62]. The calculated fiber length is reported in Table 5.3 along with the measured glass fiber lengths found in the composite before and after extrusion. The critical fiber length was found to be between 957 to 1117 μm, which is significantly larger than the measured fiber length, 612.3 μm, after printing. This confirms that the fibers will pull out of the polymer matrix rather than fracture when applied to an axial load. Another important observation is that the processing parameters used to extrude the ABS-20GF material led to a 53% reduction in fiber length as compared to the stock pellets, suggesting that the processing parameters could be further improved to minimize the reduction in fiber length and promote fiber/matrix bonding. Change in fiber length after extrusion is not unusual, process parameters such as screw speed alter the lengths substantially, as shown in the work by Ozkoc et al. [55].

Table 5.3: Measured fiber length of the ABS-20GF composite blend, before and after extrusion

	Fiber Length (μm)	Standard Deviation (±)	Critical Fiber Length (μm)
Before Processing	1148.12	226.75	957.45 - 1117.02
After Processing	612.3	168.53	

5.6 Neck Growth Variation between ABS-20GF Tensile Samples

To further investigate bead bonding, the neck growth amongst beads was analyzed. These well-defined FDM neck growth principals were applied to our BAAM printed components. The neck size was measured for layers 16 through 27 at identical

locations on the polished segments of specimens SP2 and SP5. Figure 5.9 expresses the variation of neck sizes between the specimens from the large hexagon. The average neck size for all measured layers was 2.38 mm with a standard deviation of 0.15 for SP2 and 2.33 mm with a standard deviation of 0.10 for SP5. The minimal variation of neck size among the two sample walls, spaced 1.2 m away from each other, aligns with the near identical reported tensile strengths of the coupons, this reinforces the notion that layer bonding is not affected by location across the build platform on the BAAM – 100 system.

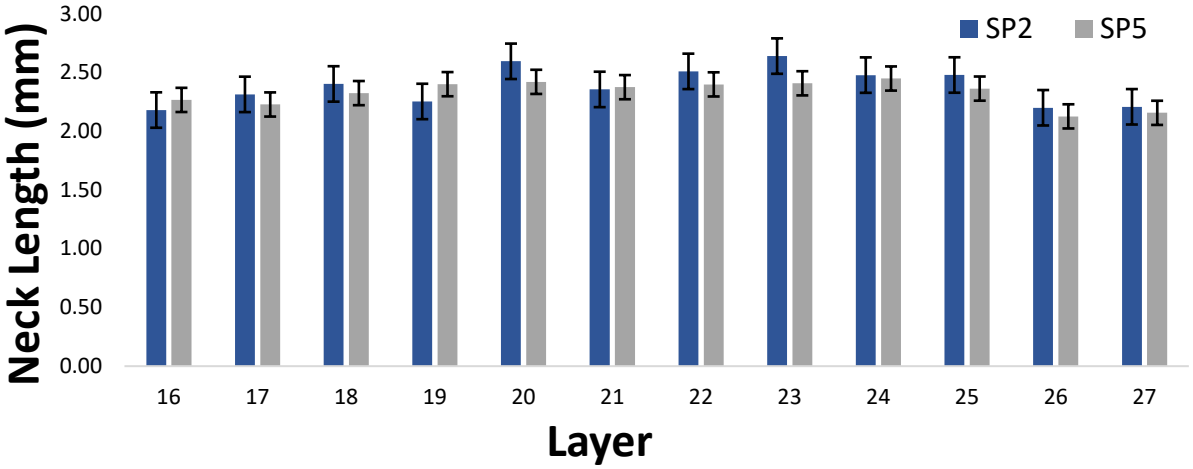

Figure 5.9: Variation of neck sizes between specimen 2 and 5 for an ABS-20GF blend

5.7 Neck Growth and Screw Speed Relationship for ABS-20CF Samples

In the previous section, the measured neck formations of the ABS-20GF hexagon demonstrated the bond quality based on the extrusion parameters used. However, in the previous study, measurements were only taking for a single set of extrusion settings. These manufacturer settings were assumed to be optimized for strength of the printed component. Although these settings could have been tailored more for dimensional accuracy instead. Thus, an additional neck growth study was carried out to determine which deposition rate (screw speed) would maximize interlayer bonding and minimize air

gaps. Due to the limited quantity of ABS-20GF pellets available, the ABS-20CF blend was used instead. Despite the difference in filler material, the findings from the study will carry over as they both are comprised of the same matrix polymer.

SEM images of the vertical cross-sections of 5 different bead samples, extruded at 50,150,250,350, and 400 rpms, are demonstrated in Figure 5.10. Large voids are easily visible in the bead cross section for the specimens printed at 250 rpms and higher, Figure 5.10(c-e). These voids are air pockets caused due to the inconsistent flow of the polymer melt when it was deposited. This signifies the limit to which the screw speed can be set to during extrusion. Bead specimens extruded at 150 rpms or less were free of any large air pockets, Figure 5.10(a-b). However, on both specimens there was evidence of small voids on the surface (see red circles). Due to the way the specimens were polished (using silicon carbide paper) it is difficult to relate the pores formed to defects caused by the screw speed used. Thus, for the continuation of the study 50 and 150 rpms were both used.

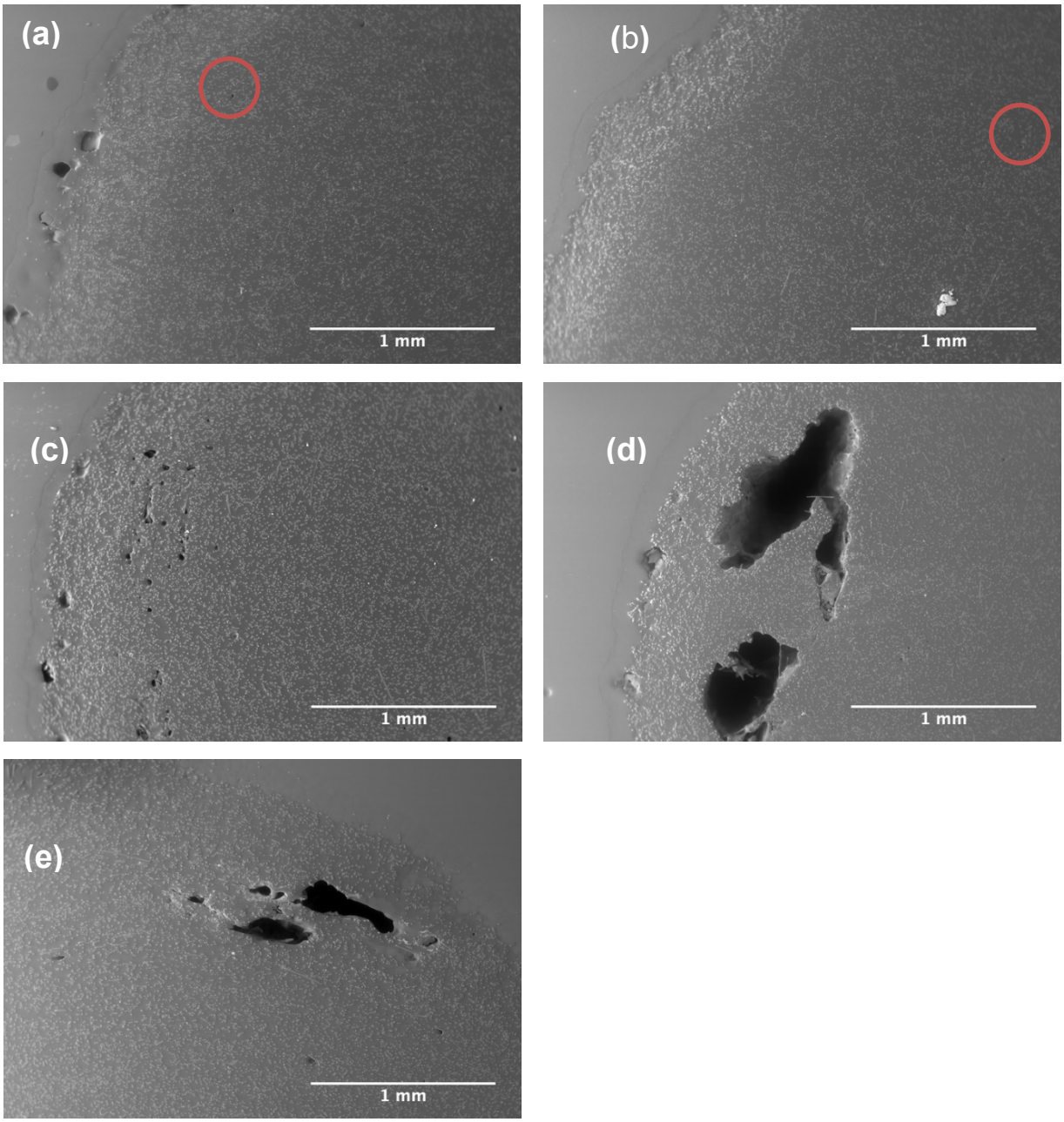

Figure 5.10: SEM images of the ABS-20CF vertical cross-sectional view extruded at 50 (a), 150 (b). 250 (c), 350 (d), and 400 rpms (e)

Neck growth measurements of the ABS-20CF were conducted in the same manner as in the previous section with the exception that the neck formation was also recorded between contour (ii) and (iii), see Figure 4.8. Figure 5.11 displays the average neck size formed among the three contours at 50 and 150 rpms. When computing the total average

of the two contours for each screw speed, the neck size was measured to be 2.40 mm ±0.31 for the specimen printed at 150 rpms and 2.15 mm ±0.27 for the specimen printed at 50 rpms. Due to the large standard deviations among the two screw speeds, any conclusions made exclusively on neck size would be insufficient. The varied neck size among beads could derive from the fact that the printed trapezoid structure was only printed with 4 layers. Any issues with bed adhesion on the initial layer would directly affect the bonding of the sequential layers. Future neck growth analysis should focus on printing specimens with a greater number of layers to avoid any distortions from the preliminary layer.

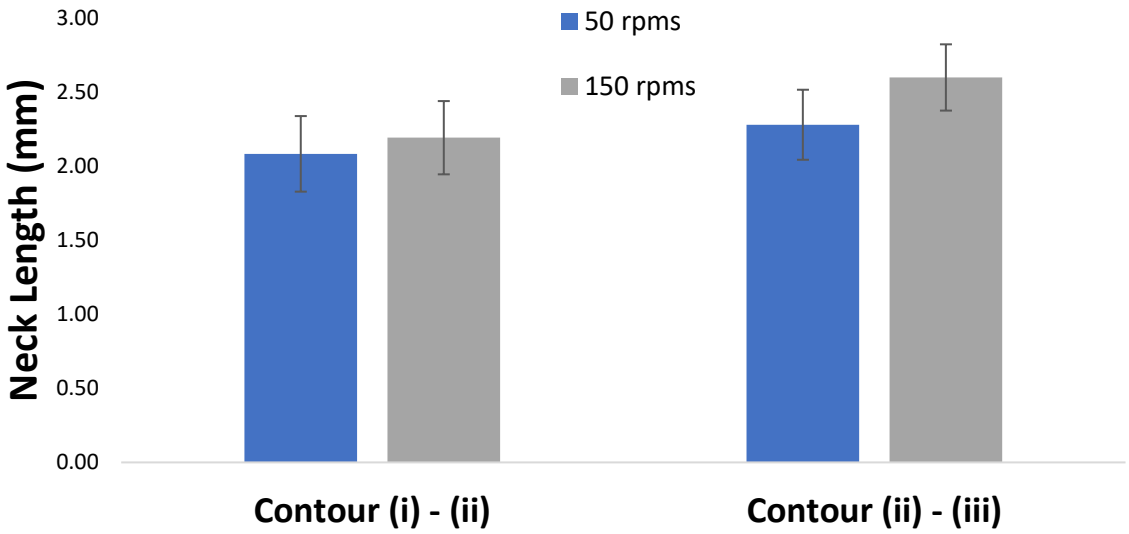

Figure 5.11: Neck size measurements of ABS-20CF specimens extruded at 50 and 150 rpms

Chapter 6: Conclusion

The work presented in this study expanded upon a previously reported method of conducting tensile tests on specimens fabricated via big area additive manufacturing (BAAM). The incorporation of DIC technology with tensile testing of large specimens was proven to be a viable technique to measure strain. DIC measurement were possible due to the development of a novel process to prepare large specimens with adequate high-contrast for displacement tracking. Recorded strain measurements were used to construct the stress-strain curves of a glass fiber (ABS-20GF) blend, marking the first one created for a BAAM printed component. The data extracted from the stress-strain curves describes the materials performance and may be used for material modeling in non-linear simulations of components with a comparable size. In addition, the acquired DIC data provided Poisson's ratio and elastic modulus measurement for glass filled ABS composite. Strain fields were shown to be consistent on all specimens,

Failure analysis on the large tensile specimens showed that the coupons failed in a brittle-like fashion with the raster gaps acting as stress concentrators. Physical fractographic evidence correlated well with DIC as the crack propagation behavior modeled by imaging matched what was observed on the fracture surface. This indicates that the DIC processes employed in this study is a reasonable method to measure strain among large test specimens. The consistency among tensile properties and the bead neck formation on the ABS-20GF specimens, signifies that bonding among beads was nearly homogenous throughout the build platform. The supplement neck growth study provided an indication that single screw extrusion ABS-20CF should be kept below 150 rpms.

While no test standard currently exists to accommodate the mechanical testing of large additively manufactured components, the work here suggests guidelines to acquire mechanical data. Therefore, contributing to the fundamental characterization of BAAM printed parts and pushing the technology one step closer toward becoming a multiprocessing additive manufacturing method.

6.1 Future Work

Future studies will continue with the manipulation of the BAAM extrusion processes to maximize interlayer bonding and minimization of air gaps. Primarily focusing on the work conducted with the ABS-20%CF to provide a more thorough investigation on the effect of screw speed with bond quality and tensile strength. This next attempt will proceed forward with the full tensile-DIC characterization of large specimens printed at both screw speeds (50 & 150 rpms). In addition, geometrical accuracy of the as printed components will be assessed at both speeds to determine the practicality of printing at higher deposition rates. The method used to coat the tensile specimen surface should be reexamined to determine an alternative that does not involve coating the entire sample with and acrylic sealant. This directly affects the tensile properties as the acrylic seals any defects on the surface and provides additional reinforcement to the component. Additionally, the spray paint used to establish the white contrast is a solvent based paint which reacts with the ABS polymer. Upon further validation of the DIC process with BAAM components, testing should move toward a new material system with superior structural application such as the use of polyetherimides.

Chapter 7: References

[1] ASTM and ISO, “Standard Terminology for Additive Manufacturing – General Principles – Terminology,” *ISO/ASTM*, vol. 52900, p. 9, 2015.

[2] S. H. Ahn, M. Montero, D. Odell, S. Roundy, and P. K. Wright, “Anisotropic material properties of fused deposition modeling ABS,” *Rapid Prototyp. J.*, vol. 8, no. 4, pp. 248–257, 2002.

[3] A. Bellini and S. Güçeri, “Mechanical characterization of parts fabricated using fused deposition modeling,” *Rapid Prototyp. J.*, vol. 9, no. 4, pp. 252–264, 2003.

[4] S. S. Crump, “Apparatus and method for creating three-dimensional objects,” 30-Oct-1989.

[5] D. A. Roberson, D. Espalin, and R. B. Wicker, “3D printer selection: A decision-making evaluation and ranking model,” *Virtual Phys. Prototyp.*, vol. 8, no. 3, pp. 201–212, Sep. 2013.

[6] C. J. Kief, E. Macdonald, C. Shemelya, D. A. Roberson, J. Aarestad, D. Roberson, R. Wicker, W. M. Keck, A. M. Kwas, M. Zemba, K. Avery, R. Netzer, and W. Kemp, “Printing Multi-Functionality: Additive Manufacturing for CubeSats Antenna Design View project Use of CNTs in advanced polymers for spacecrafts View project Printing Multi-Functionality: Additive Manufacturing for CubeSats.”

[7] C. Shemelya, L. Banuelos-Chacon, A. Melendez, C. Kief, D. Espalin, R. Wicker, G. Krijnen, and E. MacDonald, “Multi-functional 3D printed and embedded sensors for satellite qualification structures,” in *2015 IEEE SENSORS*, 2015, pp. 1–4.

[8] J. L. Coronel, K. H. Fehr, D. D. Kelly, D. Espalin, and R. B. Wicker, “Increasing component functionality via multi-process additive manufacturing,” 2017, vol. 10194, p. 101941F.

[9] C. Shemelya, F. Cedillos, E. Aguilera, E. Maestas, J. Ramos, D. Espalin, D. Muse, R. Wicker, and E. MacDonald, “3D printed capacitive sensors,” in *2013 IEEE SENSORS*, 2013, pp. 1–4.

[10] V. Kishore, C. Ajinjeru, A. Nycz, B. Post, J. Lindahl, V. Kunc, and C. Duty, “Infrared preheating to improve interlayer strength of big area additive manufacturing (BAAM) components,” *Addit. Manuf.*, vol. 14, pp. 7–12, Mar. 2017.

[11] C. E. Duty, V. Kunc, B. Compton, B. Post, D. Erdman, R. Smith, R. Lind, P. Lloyd, and L. Love, “Structure and mechanical behavior of Big Area Additive Manufacturing (BAAM) materials,” *Rapid Prototyp. J.*, vol. 23, no. 1, pp. 181–189, 2017.

[12] R. Jackson, S. Curran, P. Chambon, B. Post, L. Love, R. Wagner, B. Ozpineci, M. Chinthavali, M. Starke, J. Green, L. Tryggestad, and B. Lee, “OVERVIEW OF THE OAK RIDGE NATIONAL LABORATORY ADVANCED MANUFACTURING INTEGRATED ENERGY DEMONSTRATION PROJECT: CASE STUDY OF ADDITIVE MANUFACTURING AS A TOOL TO ENABLE RAPID INNOVATION IN INTEGRATED ENERGY SYSTEMS,” 2016.

[13] L. A. B and K. E. George, “’Weld line behaviour of polymerblends with special reference to PP/HDPE, PP/PS and HDPE/LDPE blends,” pp. 16–21, 2005.

[14] L. A. Utracki, “Development of polymer processing,” *Commer. Polym. Blends*, pp. 53–62, 1962.

[15] C. E. Pearson, “The History of the Hydraulic Extrusion Process,” *Trans. Newcom. Soc.*, vol. 21, no. 1, pp. 109–121, Jan. 1940.
[16] C. G. Gogos and Z. Tadmor, *Principles of polymer processing*. Wiley-Interscience, 2014.
[17] T. A. Osswald, *Understanding Polymer Processing*. Cincinnati, OH: Hanser, 2017.
[18] D. V. Rosato, *Extruding Plastics: A Practical Processing Handbook*. 1998.
[19] J. R. Wagner, E. M. Mount, H. F. Giles, J. R. Wagner, E. M. Mount, and H. F. Giles, “Single Screw Extruder: Equipment,” *Extrusion*, pp. 17–46, Jan. 2014.
[20] J. R. Wagner, E. M. Mount, H. F. Giles, J. R. Wagner, E. M. Mount, and H. F. Giles, “Extrusion Process,” *Extrusion*, pp. 3–11, Jan. 2014.
[21] J. R. Wagner, E. M. Mount, H. F. Giles, J. R. Wagner, E. M. Mount, and H. F. Giles, “Twin Screw Extruder Equipment,” *Extrusion*, pp. 125–148, Jan. 2014.
[22] O. A. Mohamed, S. H. Masood, and J. L. Bhowmik, “Optimization of fused deposition modeling process parameters: a review of current research and future prospects,” *Adv. Manuf.*, vol. 3, no. 1, pp. 42–53, Mar. 2015.
[23] A. Gebhardt, *Understanding Additive Manufacturing*. München: Carl Hanser Verlag GmbH & Co. KG, 2011.
[24] B. Post, P. Chesser, R. Lind, M. Sallas, and L. J. Love, “Feasibility of using Big Area Additive Manufacturing to Directly Manufacture Boat Molds,” 2018.
[25] I. Gibson, D. Rosen, and B. Stucker, “Generalized Additive Manufacturing Process Chain,” in *Additive Manufacturing Technologies*, New York, NY: Springer New York, 2015, pp. 43–61.
[26] K. L. Alvarez, R. F. Lagos, and M. Aizpun, “Investigating the influence of infill percentage on the mechanical properties of fused deposition modelled ABS parts Investigando la influencia del porcentaje de relleno en las propiedades mecánicas, de elementos impresos con ABS por el método de modelado por deposición fundida,” vol. 36, no. 3, pp. 110–116, 2016.
[27] A. Azari and S. Nikzad, “The evolution of rapid prototyping in dentistry: A review,” *Rapid Prototyp. J.*, vol. 15, no. 3, pp. 216–225, 2009.
[28] R. Singh and S. Singh, “Additive Manufacturing: An Overview,” *Ref. Modul. Mater. Sci. Mater. Eng.*, 2017.
[29] E. Kroll and D. Artzi, “Enhancing aerospace engineering students’ learning with 3D printing wind-tunnel models,” *Rapid Prototyp. J.*, vol. 17, no. 5, pp. 393–402, 2011.
[30] I. Gibson, D. Rosen, and B. Stucker, “Extrusion-Based Systems,” in *Additive Manufacturing Technologies*, New York, NY: Springer New York, 2015, pp. 147–173.
[31] Cincinnati, “2016 BAAM Fact Sheet.” Cincinnati, 2016.
[32] Cincinnati Incorporated, “OPERATION, SAFETY, AND MAINTENANCE MANUAL BAAM-100.”
[33] C. Ajinjeru, V. Kishore, J. Lindahl, Z. Sudbury, A. A. Hassen, B. Post, L. Love, V. Kunc, and C. Duty, “The influence of dynamic rheological properties on carbon fiber-reinforced polyetherimide for large-scale extrusion-based additive manufacturing,” 2018.
[34] L. J. Love, “Feasibility of Using Additive Manufacturing to Produce Automotive Tooling,” 2018.

[35] B. K. Post, B. Richardson, R. Lind, L. J. Love, P. Lloyd, V. Kunc, B. J. Rhyne, A. Roschli, J. Hannan, S. Nolet, K. Veloso, P. Kurup, T. Remo, and D. Jenne, “BIG AREA ADDITIVE MANUFACTURING APPLICATION IN WIND TURBINE MOLDS,” in *Solid Freeform Fabrication*, 2017.
[36] A. H. Peng and Z. M. Wang, “Researches into Influence of Process Parameters on FDM Parts Precision,” *Appl. Mech. Mater.*, vol. 34–35, pp. 338–343, Oct. 2010.
[37] A. Lanzotti, M. Grasso, G. Staiano, and M. Martorelli, “Rapid Prototyping Journal The impact of process parameters on mechanical properties of parts fabricated in PLA with an open-source 3-D printer Article information.”
[38] C. Bellehumeur, L. Li, Q. Sun, and P. Gu, “Modeling of Bond Formation Between Polymer Filaments in the Fused Deposition Modeling Process,” *J. Manuf. Process.*, vol. 6, no. 2, pp. 170–178, 2004.
[39] V. Francis and P. K. Jain, “Virtual and Physical Prototyping Experimental investigations on fused deposition modelling of polymer-layered silicate nanocomposite Experimental investigations on fused deposition modelling of polymer-layered silicate nanocomposite,” *Phys. Prototyp.*, vol. 11, no. 2, pp. 109–121, 2016.
[40] S. Moylan, J. Slotwinski, A. Cooke, K. Jurrens, M. A. Donmez, and A. Donmez, “Proposal for a Standardized Test Artifact for Additive Manufacturing Machines and Processes,” *Solid Free. Fabr. Symp. Proc.*, pp. 902–920, 2012.
[41] T. Brajlih, B. Valentan, J. Balic, and I. Drstvensek, “Speed and accuracy evaluation of additive manufacturing machines,” *Rapid Prototyp. J.*, vol. 17, no. 1, pp. 64–75, Jan. 2011.
[42] K. A. Ghany and S. F. Moustafa, “Comparison between the products of four RPM systems for metals,” *Rapid Prototyping Journal*, vol. 12, no. 2. Emerald Group Publishing Limited, pp. 86–94, 13-Mar-2006.
[43] M. Mahesh, Y. S. Wong, J. Y. H. Fuh, and H. T. Loh, “Benchmarking for comparative evaluation of RP systems and processes,” *Rapid Prototyping Journal*, vol. 10, no. 2. Emerald Group Publishing Limited, pp. 123–135, 13-Apr-2004.
[44] D. A. Roberson, A. R. Torrado Perez, C. M. Shemelya, A. Rivera, E. MacDonald, and R. B. Wicker, “Comparison of stress concentrator fabrication for 3D printed polymeric izod impact test specimens,” *Addit. Manuf.*, vol. 7, pp. 1–11, Jul. 2015.
[45] A. M. Forster, “Materials Testing Standards for Additive Manufacturing of Polymer Materials: State of the Art and Standards Applicability,” Gaithersburg, MD, May 2015.
[46] ASTM International, “ASTM D638 Standard test method for tensile properties of plastics,” *ASTM Int.*, vol. 08, pp. 46–58, 2003.
[47] R. Bedsole, C. Hill, K. Rowe, C. Duty, C. Ajinjeru, V. Kunc, and D. Riha, “Big Area Additive Manufacturing (BAAM) Materials Development and Reinforcement with Advanced Composites,” Knoxville, TN, 2018.
[48] B. Pan, K. Qian, H. Xie, and A. Asundi, “Two-dimensional digital image correlation for in-plane displacement and strain measurement: A review,” *Meas. Sci. Technol.*, vol. 20, no. 6, 2009.
[49] N. McCormick and J. Lord, “Digital Image Correlation,” *Mater. Today*, vol. 13, no. 12, pp. 52–54, 2010.

[50] G. H. Michler, *Atlas of Polymer Structures*. Hanser, 2016.
[51] T. Russell, B. Heller, D. Jack, and D. Smith, “Prediction of the Fiber Orientation State and the Resulting Structural and Thermal Properties of Fiber Reinforced Additive Manufactured Composites Fabricated Using the Big Area Additive Manufacturing Process,” *J. Compos. Sci.*, vol. 2, no. 2, p. 26, Apr. 2018.
[52] S. Y. Fu and B. Lauke, “Fracture resistance of unfilled and calcite-particle-filled ABS composites reinforced by short glass fibers (SGF) under impact load,” *Compos. Part A Appl. Sci. Manuf.*, vol. 29, no. 5–6, pp. 631–641, Jan. 1998.
[53] B. G. Compton, B. K. Post, C. E. Duty, L. Love, and V. Kunc, “Thermal analysis of additive manufacturing of large-scale thermoplastic polymer composites,” *Addit. Manuf.*, vol. 17, pp. 77–86, Oct. 2017.
[54] ASTM International, “ASTM D1238-13 Standard Test Method for Melt Flow Rates of Thermoplastics by Extrusion Plastometer,” 2013.
[55] G. Ozkoc, G. Bayram, and E. Bayramli, “Short glass fiber reinforced ABS and ABS/PA6 composites: Processing and characterization,” *Polym. Compos.*, vol. 26, no. 6, pp. 745–755, 2005.
[56] ASTM International, “ASTM D618-13 Standard Practice for Conditioning Plastics for Testing,” West Conshohocken, PA, 2013.
[57] A. R. Torrado and D. A. Roberson, “Failure Analysis and Anisotropy Evaluation of 3D-Printed Tensile Test Specimens of Different Geometries and Print Raster Patterns,” *J. Fail. Anal. Prev.*, vol. 16, no. 1, pp. 154–164, Feb. 2016.
[58] H. Rezayat, W. Zhou, A. Siriruk, D. Penumadu, and S. S. Babu, “Materials Science and Technology Structure-mechanical property relationship in fused deposition modelling Structure-mechanical property relationship in fused deposition modelling,” 2015.
[59] L. Engel, *An Atlas of Polymer Damage Surface Examination by Scanning Electron Microscope*. Wolfe Publishing Ltd., 1981.
[60] A. R. Torrado Perez, D. A. Roberson, and R. B. Wicker, “Fracture surface analysis of 3D-printed tensile specimens of novel ABS-based materials,” *Journal of Failure Analysis and Prevention*, vol. 14, no. 3. pp. 343–353, 2014.
[61] S.-Y. Fu, B. Lauke, E. Mäder, C.-Y. Yue, and X. Hu, “Tensile properties of short-glass-fiber-and short-carbon-fiber-reinforced polypropylene composites,” *Compos. Part A Appl. Sci. Manuf.*, vol. 31, no. 10, pp. 1117–1125, 2000.
[62] E. Pisanova and E. Máder, “Acid-base interactions and covalent bonding at a fiber-matrix interface: Contribution to the work of adhesion and measured adhesion strength,” *J. Adhes. Sci. Technol.*, vol. 14, no. 3, pp. 415–436, Jan. 2000.

Vita

Kevin Schnittker was born on January 14th in El Paso, Texas. Kevin attended Eastwood High School in El Paso and earned a high School Diploma in 2012. Immediately upon graduating, he attended the University of Texas at El Paso and pursued a degree in Metallurgical and Materials Engineering. During his undergraduate career he worked as a K-12 outreach coordinator and a research assistant in a polymer extrusion lab. Kevin received a Bachelor of Science in Metallurgical and Materials Engineering in the fall of 2015. Kevin has interned at Oak Ridge National Labs (ORNL) with the Center for Nanophase Materials Sciences and conducted research on MWCNTs. The research conducted within Dr. Roberson's polymer extrusion lab, led to a publication submitted to Virtual and Physical Prototyping titled "ABS-maleated SEBS blend as a 3D printable material". This study demonstrated the rheological effects of varying styrene ethylene butylene stryrene and acrylonitrile burtadiene styrene mixture composition.

Contact Information: Kschnittker4@gmail.com